

UNIVERSITÀ DEGLI STUDI DI TRIESTE

FACOLTÀ DI SCIENZE MATEMATICHE FISICHE E NATURALI

Corso di Laurea Magistrale in Fisica

Curriculum in Microfisica e Fisica della materia



**Design and experimental realization of a
pulsed homodyne detector for optical
quantum states characterization**

Relatore:

Dott. Daniele FAUSTI

Correlatore:

Dott. Stefano OLIVARES

Laureanda:

Martina ESPOSITO

ANNO ACCADEMICO 2011/1012

Alla mia terra, e a tutto quello che significa ...

Provare meraviglia è un requisito
scientifico, perché istiga a scoprire.

Sulla traccia di Nives

ERRI DE LUCA

Introduction

This thesis describes the realization of an experimental apparatus for the *Balanced Homodyne Detection (BHD)* of quantum states of light. This experimental technique provides a way to measure optical quantum states generated by both continuous and pulsed laser sources.

“Measuring” the quantum state of a physical system means to completely characterize the system since in this way the expectation value of all its observables can in principle be obtained.

BHD is extensively used in Quantum Optics, since it gives the unique opportunity of measuring all possible linear combinations of position and momentum of the harmonic oscillator representing a single mode of the electromagnetic radiation. From such measurement the quantum state of the single mode radiation field can be retrieved. The method as a whole is called *Optical Homodyne Tomography*.

More specifically, we realized a Balanced Homodyne Detector which works in pulsed regime; the optical states we measured are coherent states generated by a pulsed laser source which produces a train of ultrashort pulses of about 10^{-13} seconds duration.

BHD in pulsed regime is experimentally more challenging than the *BHD* based on continuous laser sources. We chose to work in a pulsed configuration in view of possible applications of this apparatus to time-resolved spectroscopy experiments: by measuring at different times the quantum state of the pulsed light after the interaction with a material, it will be possible to follow the dynamics of the excitation phenomena (for example coherent vibrational states) which can be created in the material itself. This thesis can

be regarded as the first step toward the realization of such novel experimental framework. The research project, of which this thesis constitutes the starting point, turns out to be a theoretical-experimental collaboration between the theoretical group of the Department of Physics at the University of Trieste (dr. Fabio Benatti and dr. Roberto Floreanini) and the *T-Rex* experimental group at *Elettra*-Sincrotrone in Trieste led by prof. Fulvio Parmigiani.

The thesis is divided in two parts: a theoretical part, consisting in the study of the theoretical model needed for the description of the Balanced Homodyne Detection in a pulsed regime and an experimental one which deals with the actual experimental realization and characterization of the apparatus.

The original content of the work can be regarded to be twofold: from the theoretical point of view, a mathematical framework to appropriately describe the homodyne detection in pulsed regime has been developed using the formalism of the Quantum Optics; to our knowledge, this issue has been poorly treated in the literature. From the experimental point of view, the novelty of our apparatus is that it has been realized using exclusively commercial tools for the optical pulses detection.

The thesis consists in six Chapters and three Appendixes.

Chapter 1 introduces the theoretical background needed to describe the homodyne measurements of optical quantum states, introducing the formalism of *Fock states* and *coherent states* and starting from the concept of *quantum tomography* as a technique to retrieve the state of a generic quantum system; Chapter 2 discusses the theoretical model of the *BHD* technique; Chapter 3 describes the experimental apparatus in regard to the pulsed laser source, the optomechanical set up and the acquisition system; Chapter 4 contains the presentation of all the characterization measurements of the apparatus; Chapters 5 and 6 present respectively the homodyne measurements of coherent states with different mean number of photons per pulse and the data analysis of such measurements. The mathematical formalism we developed to describe the *BHD* in quantum regime is presented in Appendixes.

Contents

Introduction	i
1 Preliminary concepts	1
1.1 The concept of quantum tomography	1
1.2 Tomography in quantum optics	5
1.3 Gaussian states	13
2 Balanced homodyne detection	17
2.1 <i>BHD</i> scheme	17
2.2 Validity of homodyne detection for quadrature measures . . .	20
2.3 Classical and quantum regimes	22
2.4 Time-domain pulsed regime	23
2.5 State of art	25
3 Experimental apparatus	27
3.1 Pulsed laser source	28
3.2 Optomechanical scheme	32
3.3 Acquisition system	34
4 Pulsed homodyne detector characterization	37
4.1 Characterization of the mechanical stability	37
4.2 Characterization of the differential acquisition system	39
4.3 Correlation test between successive pulses	47
5 Measurements	51
5.1 Homodyne measurement procedure	51
5.2 Measurements in quantum regime	54

CONTENTS

5.3	Effects of the piezo translator instability	57
6	Data analysis	59
6.1	Rescaling procedure	59
6.2	Estimation of $\langle \hat{n} \rangle$	62
6.3	Pattern function tomography	67
A	Density operator formalism	73
B	Coherent states	75
C	Homodyne detection formalism in pulsed regime	79
	Conclusions	85
	Riassunto dettagliato	87
	Bibliography	96
	Ringraziamenti	97

Chapter 1

Preliminary concepts

A physical system in Quantum Mechanics is totally described by its quantum state, in which the whole information about the system is encoded. From the experimental point of view, the challenge is to retrieve the state of a generic physical system.

Nevertheless, as for continuous variable quantum states of light, a highly efficient experimental method, called *Optical Homodyne Tomography*, exists to achieve this goal. With this technique, the quantum state of a single optical mode produced by a laser source can be totally reconstructed.

This thesis consists in the setting up of an experimental apparatus for the homodyne tomography of single-mode states of light in pulsed regime.

In this chapter we provide the theoretical background necessary for the description of the experimental scheme and the treatment of the experimental data in order to retrieve the states of light under investigation.

1.1 The concept of quantum tomography

Quantum tomography consists in the determination of the state of a quantum system. In Classical Mechanics, one can always fully recover the state of a system by a set of multiple measurements on it. In Quantum Mechanics this is not always possible, due to fundamental limitations imposed by the very nature of the theory. In fact, the Heisenberg uncertainty principle forbids to perform an arbitrary sequence of measurements on a single system without

inducing on it modifications of some sort. Moreover, the no-cloning theorem asserts that it's not possible to create a perfect copy of the system without already knowing its state in advance. Thus, in general, there is no way to infer the quantum state of a single system doing measurements on it.

Nevertheless, it is possible to estimate the unknown quantum state of a physical system when many identical copies of it are available in the same state: in this way independent measurements can be performed on each copy. Indeed, quantum tomography typically consists in several measurements performed on many ensembles of identically prepared systems, each time modifying the measurement apparatus so that different sets of data, associated with different bases, can be acquired. Then, the data are combined using reconstructional algorithms to finally get the state of the system.

The problem of quantum state determination through repeated measurements on identical copies of a quantum system was studied for the first time in 1957 by Fano [1], who recognized the need of measuring more than two non commuting observables to achieve such goal. He called "*quorum*" a set of observables whose measurements is sufficient to provide a complete determination of the state of the system.

However, the first experimental demonstration of a tomographic state reconstruction was done in the domain of Quantum Optics by Smithey et al. in 1993 [2], on the basis of the theoretical work of Vogel and Risken (1989) [3]. This 1993 paper introduced the term *tomography* into Quantum Optics and its general scheme is still used today for investigating quantum properties of continuous variable states of light.

In Quantum Optics, in fact, using a *balanced homodyne detector* (treated in detail in the next chapter), one has the unique opportunity of measuring all possible linear combinations of position and momentum of a harmonic oscillator, which here represents a single mode of the electromagnetic field. Such observables are called *field quadratures* and constitute a *quorum* of observables for the state determination of a single mode radiation field. The technique as a whole is called *Optical Homodyne Tomography (OHT)*.

The success of *OHT* promoted the development of state-reconstruction procedures in other quantum harmonic oscillator systems, such as the vibrational states of a molecule [4], or of a single trapped ion [5].

Other general methods of state reconstruction led to generalize homodyne tomography with any number of modes, and then to extend the tomographic method from the harmonic oscillator to an arbitrary quantum system using group theory [6].

Nowadays, quantum tomography is applied to a variety of quantum systems [7, 8] and constitutes a standard tool especially in the experimental implementation of Quantum Information protocols [9].

1.1.1 Density operator formalism

Quantum tomography is a method to estimate the state of a quantum system; we now specify what one means for states of a quantum system. The formalism used in Quantum Mechanics to describe the state of a generic quantum system is now presented.

Quantum states embody all what one knows about a physical system: the standard ones are the so-called *pure states* corresponding to normalized vectors $|\Psi\rangle$ in a suitable Hilbert-space \mathcal{H} .

The mean values of the system observables, Hermitian operators $A = A^\dagger$ acting on \mathcal{H} , are given by: $\langle A \rangle_\Psi = \langle \Psi | A | \Psi \rangle = \text{Tr}[A |\Psi\rangle\langle \Psi|]$. Thus, vector states can be identified by projectors $|\Psi\rangle\langle \Psi|$.

More generally, the so-called *mixed states* are described by *density matrices* $\hat{\rho}$ acting on \mathcal{H} : that is by Hermitian, non-negative Hilbert-space operators of unit-trace,

$$\hat{\rho} = \sum_i \lambda_i |\Psi_i\rangle\langle \Psi_i| \quad (1.1)$$

such that

$$\sum_i \lambda_i = 1, \quad \lambda_i > 0, \quad \langle \Psi_i | \Psi_i \rangle = 1, \quad \forall i. \quad (1.2)$$

The states of quantum systems are generic density matrices.

A state is *pure* when $\hat{\rho}$ becomes a projector on the Hilbert-space, i.e. when there is only one coefficient λ different from zero and equal to one, otherwise it is *mixed* and describes a statistical ensemble of physical systems in states $|\Psi_i\rangle\langle \Psi_i|$ with weight λ_i . In order to clarify this concept, we give an example of mixed quantum state in Appendix A.

To estimate the state of a physical system quantitatively means estimating all matrix elements of $\hat{\rho}$,

$$\rho_{jk} = \langle \Phi_j | \hat{\rho} | \Phi_k \rangle \quad (1.3)$$

in a representation of the density matrix in a given basis $\{|\Phi_i\rangle\}$. Indeed, the knowledge of all the density matrix elements (1.3) enables the observer to make the best possible statistical predictions about any future time-evolution of the system; namely the knowledge of the expectation value $\langle A \rangle_t = \text{Tr}[\hat{\rho}_t \hat{A}]$, with respect the state $\hat{\rho}_t$ at time t , of any observable \hat{A} of the system.

For example, if one considers a generic two-levels quantum system, a so called qubit, the density operator $\hat{\rho}$ will be defined in a two-dimensional Hilbert space with the standard basis $\{|0\rangle, |1\rangle\}$ (eigenstates of the Pauli matrix σ_z):

$$\hat{\rho} = \begin{pmatrix} \rho_{00} & \rho_{01} \\ \rho_{01} & \rho_{11} \end{pmatrix}; \quad (1.4)$$

the conditions for $\hat{\rho}$ to be hermitian, non negative and of unit trace are:

$$\rho_{00}, \rho_{11} \geq 0; \quad \rho_{00} + \rho_{11} = 1; \quad \rho_{01} = \rho_{10}^*; \quad \text{Det}[\hat{\rho}] \geq 0. \quad (1.5)$$

In order to determine the state of the system, it's necessary to retrieve all matrix elements in (1.4).

As for the diagonal elements, they can easily be estimated by measuring the probabilities $P(0)$ and $P(1)$ of obtaining the results 0 or 1 after a high number of measurements of the system in the standard basis. Indeed, those probabilities approach the mean values of the projectors $|0\rangle\langle 0|$ and $|1\rangle\langle 1|$:

$$\rho_{00} = \text{Tr}[\hat{\rho} |0\rangle\langle 0|], \quad \rho_{11} = \text{Tr}[\hat{\rho} |1\rangle\langle 1|]. \quad (1.6)$$

On the contrary, to obtain both real and imaginary parts of the off-diagonal elements is not so immediate.

For example, they could be obtained from the mean values of the observables

$$\frac{|0\rangle\langle 1| + |1\rangle\langle 0|}{\sqrt{2}}, \quad \frac{|0\rangle\langle 1| - |1\rangle\langle 0|}{i\sqrt{2}}. \quad (1.7)$$

This can be done performing measurements of the system in a basis different from the standard one; for instance, that of the Pauli matrix σ_x .

The operators in (1.7) together with $|0\rangle\langle 0|$ and $|1\rangle\langle 1|$ constitute a *quorum*

of observables, because, measuring them, one can completely estimate the density matrix.

Only the knowledge of all matrix elements corresponds to a complete knowledge of the state $\hat{\rho}$.

This simple example concretely shows the necessity in quantum tomography to identify a *quorum* of observables of the system and to estimate their mean values by measurements in different bases of the Hilbert space in order to retrieve, from the experimental results, the density matrix elements, that is the state of the system.

1.2 Tomography in quantum optics

After the previous brief introduction to the tomographic reconstruction of a generic quantum state, the specific case of quantum tomography of light is now presented, with particular attention to the *OHT* technique.

1.2.1 Review of Quantum Optics concepts

In quantum optics there is a perfect formal analogy between an electromagnetic field mode, characterized by a certain frequency and polarization, and a quantum harmonic oscillator, whose description is set within the framework of a infinite dimensional Hilbert space called Fock space.

A single mode of the radiation field is described by the mode operators \hat{a} and \hat{a}^\dagger , satisfying the bosonic commutation relation $[\hat{a}, \hat{a}^\dagger] = 1$.

The Fock space, in which the system lives, is spanned by the number basis $\{ |n\rangle \}_{n \in \mathbb{N}}$, formed by the eigenstates of the number operator $\hat{n} = \hat{a}^\dagger \hat{a}$, corresponding to n photons in the single mode.

The free mode-Hamiltonian is $\hat{H} = (\hat{a}^\dagger \hat{a} + \frac{1}{2})$; throughout this thesis, we use the natural units (i.e., $\hbar = 1$) and associate modes to quantum harmonic oscillators of unity mass and frequency.

It is then possible to define position- and momentum-like operators for the single mode:

$$\hat{q} = \frac{1}{\sqrt{2}}(\hat{a} + \hat{a}^\dagger), \quad \hat{p} = \frac{1}{i\sqrt{2}}(\hat{a} - \hat{a}^\dagger). \quad (1.8)$$

It is easy to see that, from the bosonic commutation relations, the operators just defined are canonically conjugated observables:

$$[\hat{q}, \hat{p}] = i, \quad (1.9)$$

and satisfy the Heisenberg uncertainty principle:

$$\Delta q \Delta p \geq \frac{1}{4}, \quad (1.10)$$

where $\Delta q = \langle \hat{q}^2 \rangle - \langle \hat{q} \rangle^2$ and $\Delta p = \langle \hat{p}^2 \rangle - \langle \hat{p} \rangle^2$ are the variances of the observables \hat{q} and \hat{p} .

So, they can be treated as position and momentum operators, even if they have nothing to do with the position and momentum of the photons but they refer to the harmonic oscillator associated to the single optical mode.

Moreover, using the complete formalism of electromagnetic field quantization [10], one can demonstrate the operators \hat{q} and \hat{p} are associated to the electric field operator in the following way:

$$\hat{E}_x(z, t) = E_0[\cos(\omega t)\hat{q} + \sin(\omega t)\hat{p}] \sin(kz), \quad (1.11)$$

where E_0 has the dimensions of an electric field. We assumed here the single mode electric field to be polarized along the x -direction while propagating along the z -direction with frequency ω and wavevector k .

The simplest example of single-mode states of the electromagnetic radiation field are the Fock states $|n\rangle$, also called **number states**, because eigenstates of the number operator:

$$\hat{n} |n\rangle = \hat{a}^\dagger \hat{a} |n\rangle = n |n\rangle. \quad (1.12)$$

They constitute an orthonormal basis of the single mode Fock space (number basis).

The ground state, known as **vacuum state**, is defined by the following action of the annihilation operator:

$$\hat{a} |0\rangle = 0, \quad (1.13)$$

while the excited states are given by:

$$|n\rangle = \frac{(\hat{a}^\dagger)^n}{\sqrt{n!}} |0\rangle. \quad (1.14)$$

The number states have a perfectly fixed photon number (n) and possess appealing physical properties, but are difficult to generate with present technology.

Another important class of single-mode states, for their physical meaning, are *coherent states* [11], which we now consider in detail.

Coherent states are eigenstates of the annihilation operator:

$$\hat{a} |\alpha\rangle = \alpha |\alpha\rangle, \quad (1.15)$$

where $\alpha \in \mathbb{C}$, because \hat{a} is not Hermitian.

The Fock vacuum is a coherent state, since it satisfies (1.15) with $\alpha = 0$.

In particular a generic coherent state can be written starting from the vacuum in the following way:

$$|\alpha\rangle = D(\alpha) |0\rangle, \quad (1.16)$$

where

$$D(\alpha) = \exp(\alpha \hat{a}^\dagger - \alpha^* \hat{a}) \quad (1.17)$$

is the single mode *displacement operator*; indeed,

$$D^\dagger(\alpha) \hat{a} D(\alpha) = \hat{a} + \alpha, \quad (1.18)$$

$$D^\dagger(\alpha) \hat{a}^\dagger D(\alpha) = \hat{a}^\dagger + \alpha^*. \quad (1.19)$$

Coherent states can be also written in the number basis [11] as:

$$|\alpha\rangle = e^{-\frac{|\alpha|^2}{2}} \sum_{n=0}^{\infty} \frac{\alpha^n}{\sqrt{n!}} |n\rangle. \quad (1.20)$$

Finally, it can be shown [12] that a coherent state is a minimum uncertainty state, so that the equality sign in equation (1.10) holds, as the uncertainties in the two observables results to be equal ($\Delta q = \Delta p = \frac{1}{2}$).

Further details about the coherent states properties are given in Appendix B. Those pure states, which like the coherent states verify the minimum uncertainty relation ($\Delta q \Delta p = 1/4$), but for which the two uncertainties are

different ($\Delta q \neq \Delta p$), are called *squeezed states*.

A quantized light field can be graphically represented using the *phasor diagram*, very popular in Quantum Optics, which plots \hat{p} versus \hat{q} . In such

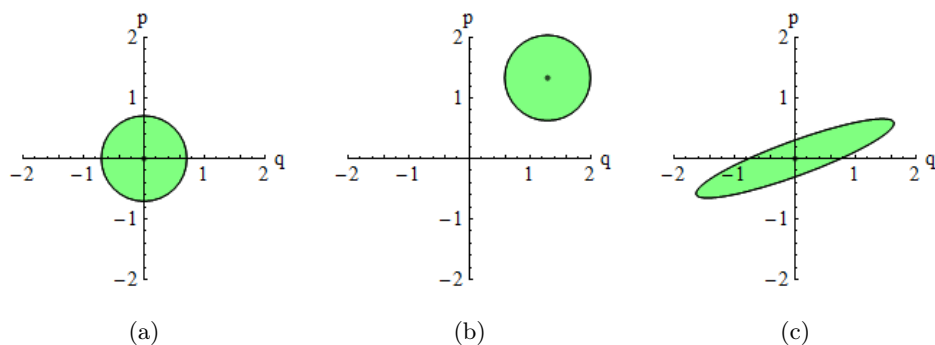


Figure 1.1: Phasor diagrams for a vacuum state (a), a coherent state (b), and a squeezed vacuum state(c) [12].

diagram any particular single mode state is equivalent to an area centered around the point given by the mean values ($\langle \hat{q} \rangle, \langle \hat{p} \rangle$). Moreover, the size of the area is given by the square root of the variances: $\sqrt{\Delta q}$ and $\sqrt{\Delta p}$.

Using these graphics, to note the differences between vacuum, coherent and squeezed single mode optical states is immediate (Figure 1.1).

1.2.2 Optical homodyne tomography

Optical homodyne tomography is a specific technique for characterizing quantum states of light by measuring a series of continuous-spectrum observables \hat{x}_Φ , called *field quadratures*, for different $\Phi \in [0, 2\pi]$.

This set of observables constitutes a *quorum*, whose measurement provide tomographically complete information about the quantum state.

For a single mode radiation field, these continuous degrees of freedom are defined by generalizing equations (1.8):

$$\hat{x}_\Phi = \frac{1}{\sqrt{2}}(\hat{a}e^{-i\Phi} + \hat{a}^\dagger e^{i\Phi}), \quad (1.21)$$

Position- and momentum-like operator (1.8) are obtained for $\Phi = 0$ and $\Phi = \pi/2$, respectively:

$$\begin{cases} \hat{x}_0 = \frac{1}{\sqrt{2}}(\hat{a} + \hat{a}^\dagger) = \hat{q} \\ \hat{x}_{\pi/2} = \frac{1}{i\sqrt{2}}(\hat{a} - \hat{a}^\dagger) = \hat{p} \end{cases} \quad (1.22)$$

In the quantum optical formalism, these observables can also be considered as linear combinations of the position and momentum of the harmonic oscillator associated to the optical mode: $\hat{x}_\Phi = \hat{q} \cos \Phi + \hat{p} \sin \Phi$. The eigenstates $|x_\Phi\rangle$ of the quadrature operator for each Φ can be written in the number basis as:

$$|x_\Phi\rangle = \frac{e^{-\frac{1}{2}x^2}}{\sqrt[4]{\pi}} \sum_{n=0}^{\infty} \frac{H_n(x)}{\sqrt{2^n n!}} e^{-in\Phi} |n\rangle, \quad (1.23)$$

where $H_n(x)$ is the n -th Hermite polynomial.

They constitute a complete system of eigenstates ($\int_{\mathbb{R}} dx_\Phi |x_\Phi\rangle \langle x_\Phi| = 1 \forall \Phi$). The measurements of the field quadrature \hat{x}_Φ are provided by means of an experimental apparatus called *balanced homodyne detector (BHD)*.

In a typical *BHD*, the field under study, called *signal*, interferes at a 50% *beam-splitter* with a strong coherent reference beam, called *Local Oscillator (LO)*. The outputs are collected by two photodiodes and the difference in the produced photocurrents results to be proportional to the field quadrature expectation value x_Φ , where Φ is defined by the phase of the *LO* with respect to the *signal* and can be easily varied changing the length of the *LO* optical path. A more detailed description of the homodyne detection apparatus is given in the next chapter.

Repeated homodyne measurements on identically prepared light mode in the state $\hat{\rho}$ are performed to obtain an experimental histogram which approaches the probability distribution of the quadrature outcome at a fixed phase:

$$p(x, \Phi) = \text{Tr}[\hat{\rho} |x_\Phi\rangle \langle x_\Phi|] = \langle x_\Phi | \hat{\rho} | x_\Phi \rangle. \quad (1.24)$$

This is the probability of having outcome x when measuring \hat{x}_Φ . The procedure is repeated for different phases $\Phi \in [0, 2\pi]$.

The actual tomography is the technique that from such set of experimental data leads one to completely characterize the quantum state by reconstructing

its density matrix $\hat{\rho}$ or equivalently its *Wigner function* $W[\hat{\rho}]$.

The Wigner function is a *c-number quasi-probability* distribution, i.e. it is normalized but it can generally also assume negative values [9]. For a single mode optical field it is defined as:

$$W[\hat{\rho}](z) = \int_{\mathbb{C}} \frac{d^2\lambda}{\pi^2} \exp\{i(\lambda^*z + z^*\lambda)\} \text{Tr}[D(\lambda)\hat{\rho}], \quad (1.25)$$

where $z = \frac{1}{\sqrt{2}}(q + ip)$ and $D(\lambda)$ is the displacement operator defined in the equation (1.17).

The knowledge either of the Wigner distribution or of the density matrix is equivalent to knowing the quantum state of the system under investigation. In the first quantum tomography experiment by Smithely and his group [2], a set of probability distributions for the quadrature of coherent and squeezed states of light was measured. These histograms were inverted using the *inverse Radon transform* to yield the reconstructed Wigner function of the states (Figure 1.2).

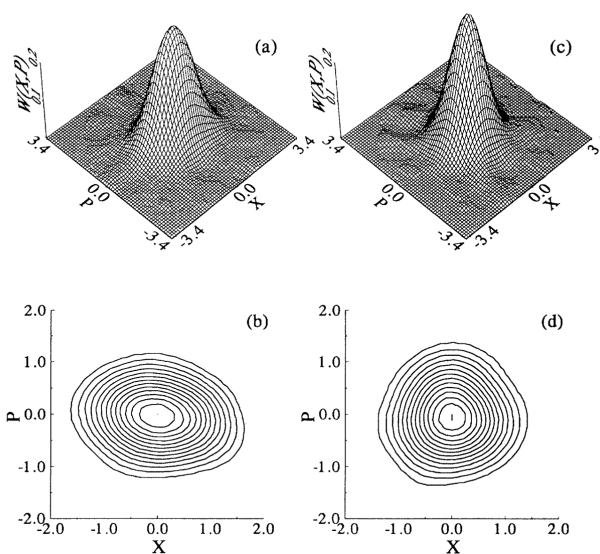


Figure 1.2: Image from [2]. Measured Wigner functions for a squeezed state (a-b) and vacuum state (c-d) viewed in 3D and as contour plot. The reconstruction is performed by using inverse Radon transformation.

The Radon transform is an algorithm usually adopted in medical tomography;

the main idea at the basis is to recover a two-dimensional (mass) distribution from one-dimensional projections in different directions. This explains the origin of the term *tomography*, from the Greek word $\tau\omicron\mu\omicron\varsigma = \textit{slice}$, which describes a method to infer an unknown object from its *projections* under various angles. Quantum tomography is the application of this idea to quantum mechanics.

According to theoretical work of Vogel and Risken ([3]), the probability distribution $p(x, \Phi)$, at a fixed phase Φ , is equal to the marginal distribution of the Wigner function $W[\hat{\rho}](q, p) = W[\hat{\rho}](z \equiv \frac{q+ip}{\sqrt{2}})$:

$$p(x, \Phi) = \int_{\mathbb{R}} dp W[\hat{\rho}](q \cos \Phi - p \sin \Phi, q \sin \Phi + p \cos \Phi). \quad (1.26)$$

In Figure 1.3 the marginal distribution of the Wigner function of a squeezed state is shown.

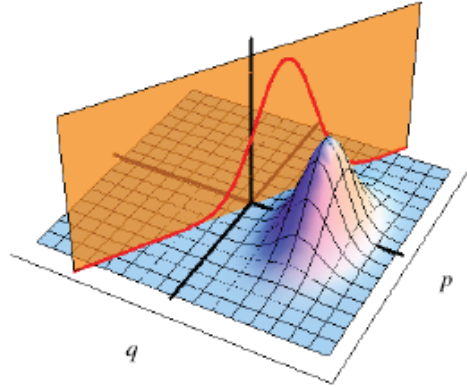


Figure 1.3: Marginal distribution of a Wigner function onto a plane rotated of a Φ angle with respect the q axis [13].

Therefore, in the experiment by Smithely, once have been measured a sufficient number of quadrature distributions $p(x, \Phi)$ for different values of Φ , it was possible to reconstruct the Wigner function using the inverse Radon transform.

This first tomographic method [2] was very important for the historical development of quantum tomography, but it was unreliable for the reconstruction of an unknown quantum state, since arbitrary smoothing parameters were needed in the Radon-transform based imaging procedure.

Subsequent more and more reliable reconstructional algorithms were proposed after 1993, when the studies in quantum-state reconstruction boomed.

The first exact unbiased tomographic method was the **pattern function tomography**, proposed in Ref. [14], and successively simplified in Ref. [15]. Unlike the Radon transform, this method allows the reconstruction of the quantum state bypassing the need of the Wigner function, and achieving the expectation value of any arbitrary operator by just averaging suitable estimators (also called *kernel functions* or *pattern functions*), evaluated from the experimental homodyne data ([6]).

A more detailed description of the pattern function tomography will be given in Section (6.3), where this technique will be used to analyse the experimental results.

In this section we focused on the Optical Homodyne Tomography description, which it is the technique used in our experiment for the characterization of continuous variable (CV) optical states. For the sake of completeness, it's important to point out the possibility to perform tomography also for discrete variable quantum states of light, that is of measuring discrete spectrum degrees of freedom of light.

An example is the polarization degree of freedom of photons emitted by a single-photon source. In this case the state of the system lives in a two-dimensional Hilbert space, indeed each polarization state can be written as a linear combination of two basis vectors, such as the vertical and horizontal polarization states or the left- and right-circular ones. This kind of *two-states* quantum-mechanical systems are called *quantum bits* (qubits) and are the quantum analogue of the classical bits in Quantum Information.

In addition to the polarization state of a single photon, several physical implementations of qubits can be realized with the actual technology, such as the spin state of an electron or the energetic state of a two-level atom and so on. In these cases, other experimental techniques exist for the *qubits tomography* [16].

1.3 Gaussian states

A particularly useful class of continuous-variables (*CV*) states in Quantum Optics are Gaussian states, defined by Gaussian Wigner functions.

The electrodynamic vacuum is itself a Gaussian state and most of the states generated in laboratory are Gaussian [9]. The optical states used in our experiment are Gaussian too.

The most general single mode Gaussian state can be always written as:

$$\hat{\rho} = \hat{\rho}(\alpha, \xi, N) = D(\alpha) S(\xi) \hat{\nu}_{th}(N) S^\dagger(\xi) D^\dagger(\alpha), \quad (1.27)$$

where $D(\alpha)$ is the displacement operator defined in the (1.17),

$$S(\xi) = \exp\left[\frac{1}{2}(\xi \hat{a}^{\dagger 2} - \xi^* \hat{a}^2)\right] \quad (1.28)$$

is the single mode *squeezing operator* and

$$\hat{\nu}_{th}(N) = \frac{e^{-\beta \hbar \omega \hat{a}^\dagger \hat{a}}}{\text{Tr}[e^{-\beta \hbar \omega \hat{a}^\dagger \hat{a}}]} = \frac{N^{\hat{a}^\dagger \hat{a}}}{(1+N)^{\hat{a}^\dagger \hat{a} + 1}} \quad (1.29)$$

$$= \frac{1}{(1+N)} \sum_{n=0}^{\infty} \left(\frac{N}{1+N}\right)^n |n\rangle \langle n| \quad (1.30)$$

is the ***thermal state***, where $\beta = 1/(k_B T)$, k_B is the Boltzmann constant, and $N = 1/(e^{\beta \hbar \omega} - 1)$ is the average number of photons in the state; $\hat{\nu}_{th}(N)$ describes a thermal equilibrium state at temperature T .

For example, if $\xi = 0$ and $N = 0$, the Gaussian state (1.27) is reduced to a coherent state (1.20) $\hat{\rho} = |\alpha\rangle \langle \alpha|$, which is the vacuum for $\alpha = 0$; while, for $\alpha = 0$, $N = 0$ and $\xi \neq 0$ one obtains the squeezed vacuum.

The Gaussian states can be theoretically dealt with in a standard way. Indeed, it is possible to define two quantities, the *first-moments vector* $\hat{\mathbf{R}} = (\hat{q}, \hat{p})^T$ and the *covariance matrix* CM $\boldsymbol{\sigma}$, that fully characterize such states and directly depend on the field quadratures.

The CM elements are given by:

$$[\boldsymbol{\sigma}]_{kj} = \frac{1}{2} \langle \{\hat{R}_k, \hat{R}_j\} \rangle - \langle \hat{R}_j \rangle \langle \hat{R}_k \rangle, \quad (1.31)$$

where $\{\hat{A}, \hat{B}\} = \hat{A}\hat{B} + \hat{B}\hat{A}$ is the anticommutator between two operators and $\langle \hat{A} \rangle = \text{Tr}[\hat{\rho}\hat{A}]$ the expectation value of the operator \hat{A} on the state $\hat{\rho}$.

For a generic state (1.27) with $\alpha = ae^{i\phi}$ and $\xi = re^{i\psi}$, the explicit expressions of the *CM* elements are:

$$\sigma_{kk} = \frac{1 + 2N}{2} [\cosh(2r) - (-1)^k \sinh(2r) \cos \psi], \quad (k = 1, 2) \quad (1.32)$$

$$\sigma_{12} = \sigma_{21} = \frac{1 + 2N}{2} \sinh(2r) \sin \psi, \quad (1.33)$$

while the first-moments vector is given by:

$$\langle \hat{\mathbf{R}} \rangle = \sqrt{2}(\Re[\alpha], \Im[\alpha])^T = \sqrt{2}(a \cos \phi, a \sin \phi)^T. \quad (1.34)$$

With this notation, one can easily write the Wigner function (1.25) of the generic single mode Gaussian state (1.27):

$$W[\hat{\rho}](z) = W[\hat{\rho}](\mathbf{X}) = \frac{\exp\{-\frac{1}{2}(\mathbf{X} - \langle \hat{\mathbf{R}} \rangle)^T \boldsymbol{\sigma}^{-1}(\mathbf{X} - \langle \hat{\mathbf{R}} \rangle)\}}{\pi \sqrt{\det[\boldsymbol{\sigma}]}} \quad (1.35)$$

where $z = \frac{1}{\sqrt{2}}(q + ip)$ and $\mathbf{X} = (q, p)^T \in \mathbb{R}^2$.

The equation (1.35) is the expression of the Wigner function in the phase space (q, p) . It is a sort of extension of a classical phase space distribution function to a quantum one, in which the variables are the eigenvalues q and p of the position- and momentum-like operators.

It is important to note that in the quantum domain, due to the commutation relations (1.9) between \hat{q} and \hat{p} , the Wigner quasi-probability function is not a genuine phase space distribution as in the classical case. Indeed, it can also assume negative values, as for the Fock states $|n\rangle$ with $n > 0$.

Since (1.35) is a Gaussian function, the state $\hat{\rho}$ is fully characterized by its *CM* $\boldsymbol{\sigma}$ and by its first-moments vector $\hat{\mathbf{R}}$.

Thus, it is natural to consider time-evolutions of a Gaussian state as transformations of these parameters ($\boldsymbol{\sigma}$ and $\hat{\mathbf{R}}$) in such a way to preserve the commutation relations $[q, p] = i$.

It can be shown that, in order to preserve the Gaussian character of a state during its evolution, the evolution Hamiltonian has to be linear or bilinear in the field mode [9].

This is the basic reason for the fundamental role of Gaussian states in quantum optics, because most of the quantum evolutions achievable with current technology, and implementable in laboratories, are actually described by Hamiltonian operators at most bilinear in the field mode and all the states produced in laboratory are evolutions of the vacuum state that is itself a Gaussian state. Gaussian states are also interesting for their “extremality” property [17].

Thus, the continuous variable states of light commonly studied in quantum optics laboratories are Gaussian and evolve preserving this character.

Moreover, one can easily characterize a Gaussian state by reconstructing its CM (1.31) by the measurements of the field quadratures with a balanced homodyne detector.

In the figure (1.4) the Wigner functions of some characteristic gaussian states are shown.

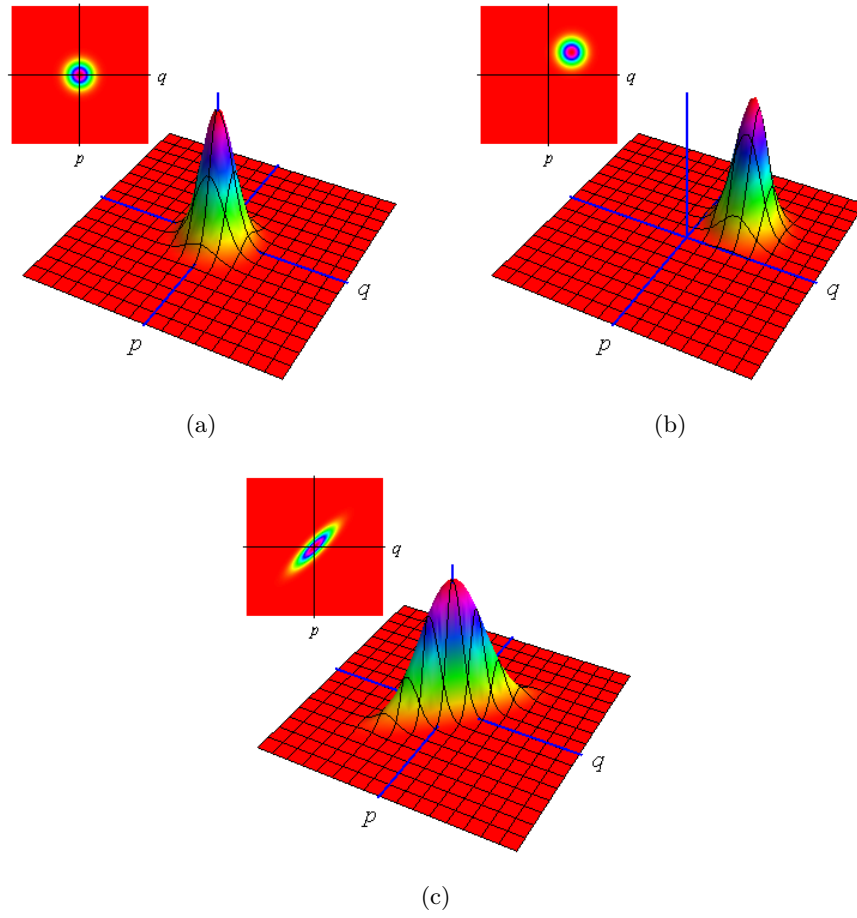


Figure 1.4: Wigner function and its projection for a vacuum state (a), a coherent state ($\alpha = ae^{i\phi}$, $a = 2$, $\phi = \pi/4$) (b), and a squeezed vacuum state ($\xi = re^{i\psi}$, $r = 0.7$, $\psi = \pi/2$) (c) [12].

Chapter 2

Balanced homodyne detection

If one knows the statistics of the field quadratures \hat{x}_Φ (1.21) with $\Phi \in [0, 2\pi]$, then it is possible to reconstruct the quantum state $\hat{\rho}$ of a single mode radiation field.

Balanced homodyne detection (*BHD*) is an experimental technique that provides the measurement of such single-mode quadratures through the mixing of the field under investigation, called *signal*, with a highly excited semiclassical field (e.g. a laser beam) at the same frequency, called *local oscillator* (*LO*). The *signal* and the *LO* are generated by a common source, so they have a fixed phase relation.

In this chapter a theoretical analysis of the *BHD* technique in pulsed regime (pulsed laser source) is presented.

2.1 *BHD* scheme

The schematic diagram of a balanced homodyne detector is reported in Fig. (2.1). The *signal* mode a is in the state $\hat{\rho}_s$ under investigation, it interferes with a second mode b (*LO*) excited in a coherent state $|z\rangle$ with $z \in \mathbb{C}$.

The detection technique is called *balanced* because the interference between the two modes happens in a balanced (50/50) *beam splitter* (*BS*).

A beam splitter is an optical device composed of a dielectric plate that produces the mixing of the two incident optical modes a and b .

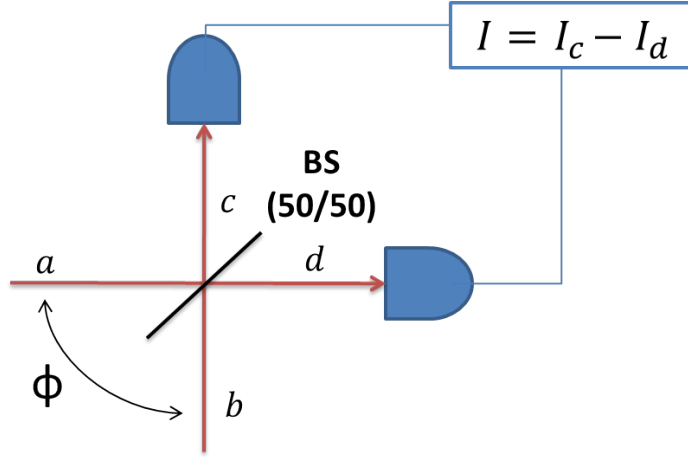


Figure 2.1: Schematic diagram of a balanced homodyne detector.

In general, a beam splitter is described by a unitary evolution operator:

$$U_{BS}(\eta) = \exp(\eta \hat{a}^\dagger \hat{b} - \eta^* \hat{a} \hat{b}^\dagger), \quad (2.1)$$

where $\eta = |\eta|e^{i\chi} \in \mathbb{C}$ is proportional to the interaction time and to the linear susceptibility of the medium.

The Heisenberg evolution of the modes a and b under the action of U_{BS} is:

$$U_{BS}^\dagger(\eta) \begin{pmatrix} \hat{a} \\ \hat{b} \end{pmatrix} U_{BS}(\eta) = \mathbf{B}(\eta) \begin{pmatrix} \hat{a} \\ \hat{b} \end{pmatrix} \quad (2.2)$$

where

$$\mathbf{B}(\eta) = \begin{pmatrix} \cos |\eta| & e^{i\chi} \sin |\eta| \\ -e^{i\chi} \sin |\eta| & \cos |\eta| \end{pmatrix}. \quad (2.3)$$

In particular, for a 50/50 BS , used in the BHD , the parameters of the evolution operator 2.1 are $\chi = 0$ and $|\eta| = \pi/4$, so the action of a 50/50 BS on the incident modes a and b is the following:

$$\begin{cases} \hat{a} \longrightarrow \hat{c} = (\hat{a} + \hat{b})/\sqrt{2} \\ \hat{b} \longrightarrow \hat{d} = (\hat{b} - \hat{a})/(\sqrt{2}) \end{cases}, \quad (2.4)$$

where \hat{c} and \hat{d} are the output mode operators.

After the BS , the two modes are detected by two identical photodetectors,

the two photocurrents are measured and subtracted from each other. The photocurrents I_c and I_d are the measured values of the the photon number observables $\hat{n}_c = \hat{c}^\dagger \hat{c}$ and $\hat{n}_d = \hat{d}^\dagger \hat{d}$.

The difference photocurrent \hat{I} is associated to the photon number difference operator between the two output channels:

$$\hat{I} = \hat{n}_c - \hat{n}_d = \hat{c}^\dagger \hat{c} - \hat{d}^\dagger \hat{d}, \quad (2.5)$$

which, using the transformations (2.4), becomes:

$$\hat{I} = \hat{a}^\dagger \hat{b} + \hat{b}^\dagger \hat{a}. \quad (2.6)$$

The phase difference between the *LO* and the *signal* can be varied changing the length of the *LO* optical path; this means that the *LO* modes are subjected to the following phase shift:

$$\begin{aligned} \hat{b} &\rightarrow \hat{b} e^{i\Phi} \\ \hat{b}^\dagger &\rightarrow \hat{b}^\dagger e^{-i\Phi}. \end{aligned} \quad (2.7)$$

We now define the homodyne photocurrent operator as:

$$\hat{I}_\Phi = \hat{a}^\dagger \hat{b} e^{i\Phi} + \hat{b}^\dagger \hat{a} e^{-i\Phi}, \quad (2.8)$$

which is the observable actually measured by a balanced homodyne detector. Now the natural question is: how, measuring the homodyne photocurrent \hat{I}_Φ , can one obtain a value for the quadrature \hat{x}_Φ of the *signal* field for a fixed phase shift Φ of the *LO* mode?

The answer comes from the fact that the expectation value of the homodyne photocurrent \hat{I}_Φ on the total input state $\hat{\rho}_s \otimes |z\rangle\langle z|$ is proportional to the expectation value of the field quadrature \hat{x}_Φ defined in (1.21):

$$\begin{aligned} \langle \hat{I}_\Phi \rangle &= \text{Tr} \left[\hat{\rho}_s \otimes |z\rangle\langle z| \hat{I}_\Phi \right] = \text{Tr} \left[\hat{\rho}_s \otimes |z\rangle\langle z| (\hat{a}^\dagger \hat{b} e^{i\Phi} + \hat{b}^\dagger \hat{a} e^{-i\Phi}) \right] \\ &= \text{Tr} \left[\hat{\rho}_s \otimes |z\rangle\langle z| (\hat{a}^\dagger \hat{b} e^{i\Phi}) \right] + h.c. = \left(\text{Tr}[\hat{\rho}_s \hat{a}^\dagger] \cdot \text{Tr}[|z\rangle\langle z| \hat{b} e^{i\Phi}] \right) + h.c. \\ &= \left(\text{Tr}[\hat{\rho}_s \hat{a}^\dagger] \cdot \langle z|\hat{b} e^{i\Phi}|z\rangle \right) + h.c. = \left(\text{Tr}[\hat{\rho}_s \hat{a}^\dagger] \cdot z e^{i\Phi} \right) + h.c. \\ &= \text{Tr} \left[\hat{\rho}_s (\hat{a}^\dagger z e^{i\Phi} + \hat{a} z^* e^{-i\Phi}) \right] = |z| \text{Tr} \left[\hat{\rho}_s (\hat{a}^\dagger e^{i\Phi} + \hat{a} e^{-i\Phi}) \right] \\ &= \sqrt{2} |z| \langle \hat{x}_\Phi \rangle, \end{aligned} \quad (2.9)$$

where we absorbed the argument of z ($\arg[z]$) in the phase Φ and we considered:

$$\langle \hat{x}_\Phi \rangle = \text{Tr}[\hat{\rho}_s \hat{x}_\Phi]. \quad (2.10)$$

A *BHD* thus measures the quadrature components \hat{x}_Φ rescaling the measured \hat{I}_Φ by a factor ($\sqrt{2}|z|$). Redefining the homodyne photocurrent \hat{I}_Φ including the rescaling factor, its expectation value coincides now with the quadratures's one:

$$\hat{I}_\Phi = \frac{\hat{a}^\dagger \hat{b} e^{i\Phi} + \hat{b}^\dagger \hat{a} e^{-i\Phi}}{\sqrt{2}|z|}. \quad (2.11)$$

The reference phase Φ is provided by the *LO* mode phase shift and can be varied experimentally, using, for instance, a piezo-electrically movable mirror which changes the LO optical path. Therefore one can obtain the statistics of the homodyne photocurrent \hat{I}_Φ for different values of $\Phi \in [0, \pi]$.

One can ensure that this statistics coincides with the one of the quadrature \hat{x}_Φ , only under some conditions on the *LO*. In particular the latter has to be in a strong semiclassical state. This fundamental point is treated in the following section.

2.2 Validity of homodyne detection for quadrature measures

To study the validity of the homodyne detection for measurements of the quadrature \hat{x}_Φ , one has to study the conditions needed to consider a measurement of the observable \hat{I}_Φ , defined in (2.11), as a good measurement of the quadrature.

The first thing to note is that the operator \hat{I}_Φ has a discrete spectrum, that coincide with the set \mathbb{Z} of relative integers. It approaches the real axis only in the limit of highly excited *LO* ($|z| \gg 1$).

In this limit, the local oscillator is excited in a strong semiclassical state such that one can consider it powerful enough to be treated classically, its quantum fluctuations can be totally neglected and the following substitutions

can be done:

$$\begin{cases} \hat{b} & \longrightarrow z \\ \hat{b}^\dagger & \longrightarrow z^*. \end{cases} \quad (2.12)$$

Using the (2.12), that is treating the LO classically, it's easy to note the equality between the homodyne photocurrent mean value $\langle \hat{I}_\Phi \rangle$ and the mean value of the field quadrature \hat{x}_Φ defined in the equation (1.21):

$$\langle \hat{I}_\Phi \rangle = \left\langle \frac{(\hat{a}^\dagger e^{i\Phi} + \hat{a} e^{-i\Phi})}{\sqrt{2}} \right\rangle = \langle \hat{x}_\Phi \rangle. \quad (2.13)$$

Nevertheless, one can observe that the moments of order greater than one of the homodyne photocurrent \hat{I}_Φ (2.11) are different from the quadrature moments.

Indeed, for the second order moment we have:

$$\begin{aligned} \langle \hat{I}_\Phi^2 \rangle &= \frac{1}{2|z|^2} \text{Tr}[\hat{\rho} \otimes |z\rangle\langle z| (\hat{a}^\dagger \hat{b} e^{i\Phi} + \hat{b}^\dagger \hat{a} e^{-i\Phi})^2] \\ &= \text{Tr}[\hat{\rho} \otimes |z\rangle\langle z| (\hat{x}_\Phi^2 + \frac{\hat{a}^\dagger \hat{a}}{2|z|^2})] \\ &= \langle \hat{x}_\Phi^2 \rangle + \left\langle \frac{\hat{a}^\dagger \hat{a}}{2|z|^2} \right\rangle. \end{aligned} \quad (2.14)$$

The following results can be proved [9] in general for all the moments of the homodyne photocurrent:

$$\begin{aligned} \langle \hat{I}_\Phi \rangle &= \langle \hat{x}_\Phi \rangle, & \langle \hat{I}_\Phi^2 \rangle &= \langle \hat{x}_\Phi^2 \rangle + \left\langle \frac{\hat{a}^\dagger \hat{a}}{2|z|^2} \right\rangle, \\ \dots & & \langle \hat{I}_\Phi^n \rangle &= \left\langle \hat{x}_\Phi^{2n-2} \left(\hat{x}_\Phi^2 + \frac{\hat{a}^\dagger \hat{a}}{2|z|^2} \right) \right\rangle. \end{aligned} \quad (2.15)$$

They coincide with the quadrature moments only when the *signal* in the mode a satisfies the condition

$$\langle \hat{a}^\dagger \hat{a} \rangle \ll |z|^2. \quad (2.16)$$

In this limit the distribution of the outcomes I_Φ of the homodyne photocurrent is equal to that of the corresponding field quadrature [9]. In all the calculations before $\arg[z]$ was absorbed in the phase Φ .

In conclusion, the balanced homodyne detector achieves the ideal measurement of the quadrature \hat{x}_Φ in the strong *LO* regime. This limit can be expressed by the two following conditions:

$$\begin{aligned} i) \quad & |z| \gg 1 \\ ii) \quad & |z|^2 \gg \langle \hat{a}^\dagger \hat{a} \rangle. \end{aligned} \tag{2.17}$$

The first guarantees the continuous spectrum of the homodyne photocurrent \hat{I}_Φ . The second neglects extra terms in the photocurrents moments. Under these conditions the probability distribution of the output photocurrent \hat{I}_Φ approaches the probability distribution $p(x, \Phi) = \langle x_\Phi | \rho | x_\Phi \rangle$ of the quadrature \hat{x}_Φ for the *signal* mode a and the fixed phase Φ .

2.3 Classical and quantum regimes

For *classical regime* of the homodyne measurement process we intend the case in which both the input modes in the Figure (2.1) are in a strong semiclassical state, i.e. when two highly excited coherent states, with a fixed phase relation between each other, interfere on the 50/50 BS.

Let's consider, for the mode a and b respectively, the coherent states $|\alpha\rangle$ ($\alpha = |\alpha|e^{i\theta}$) and $|z\rangle$ ($z = |z|e^{i\xi}$) with very large amplitudes $|\alpha|$ and $|z|$.

From the definition (1.15) of a coherent state, we know that:

$$\hat{a}|\alpha\rangle = \alpha|\alpha\rangle, \quad \hat{b}|z\rangle = z|z\rangle. \tag{2.18}$$

In this case, the measured values of the homodyne photocurrent operator, defined in the (2.8), contain information about the phase difference between the two coherent states. Indeed, using (2.18) it is easy to verify that:

$$\begin{aligned} \langle \hat{I}_\Phi \rangle &= \text{Tr}[|\alpha\rangle\langle\alpha| \otimes |z\rangle\langle z| \hat{I}_\Phi] = \langle\alpha|\langle z| (\hat{a}^\dagger \hat{b} e^{i\Phi} + \hat{b}^\dagger \hat{a} e^{-i\Phi}) |z\rangle|\alpha\rangle \\ &= z\alpha^* e^{i\Phi} + z^* \alpha e^{-i\Phi} = 2|z||\alpha| \cos \Phi, \end{aligned} \tag{2.19}$$

where the phases $\xi = \arg[z]$ and $\theta = \arg[\alpha]$ were absorbed in Φ .

This kind of detection, with two classical fields as input states, is a preliminary measurement, fundamental to verify the performance of the experimental apparatus before attenuating the *signal* beam to reach the *quantum regime*. For *quantum regime* we intend the conditions in which the *signal* field quadrature

can be reasonably estimated through measurements of the homodyne photocurrent \hat{I}_Φ . In order to reach the *quantum regime* the *signal* is attenuated using neutral filters, whose attenuation action is the following:

$$|\alpha\rangle \rightarrow |\epsilon\alpha\rangle, \quad (2.20)$$

where $0 < \epsilon < 1$.

Since in a Balanced Homodyne Detection the *signal* and the *LO* come from the same laser source, we can consider $\alpha = z$. Using these considerations and the equation (2.19), the homodyne photocurrent expectation value in *quantum regime*, i.e. when the signal is attenuated, results:

$$\langle \hat{I}_\Phi \rangle = 2\epsilon |z|^2 \cos \Phi. \quad (2.21)$$

2.4 Time-domain pulsed regime

BHD was originally designed for measurements in frequency-domain, for evaluating field quadrature noise at definite detection frequencies.

Frequency-domain detection was used, for example, to observe quadrature squeezing ([18]).

Using a frequency-domain approach, one can study a field state in the continuum wave (cw) regime, by observing a certain spectral component of the homodyne photocurrent (2.5) using an electronic spectral analyzer.

In the time-domain regime, on the contrary, the *signal* and the *LO* are provided by pulsed laser and the homodyne photocurrent, for each laser pulse, is singularly electronically integrated. The measured photon number differences, for each pulse, are used to build-up the field quadrature distribution.

Both these schemes (frequency- and time-domain) have been used to produce tomographic reconstructions, but, in order to investigate states of light with stronger non classical features, time-domain pulsed regime is necessary.

Indeed, with the time-domain approach, one can exploit the higher non linear effects caused by the high peak intensities of pulsed laser. Moreover, the time-domain provides a synchronization clock which gives the opportunity to apply the homodyne tomographic technique to *pump and probe experiments* in order to study coherent vibrational states in materials.

However, constructing a *BHD* in the time domain regime (in which the *signal* and the *LO* are both pulsed light) is more technically challenging than in the frequency-domain. The main reasons are:

- The electronics must be fast enough to ensure temporal separation of responses to individual laser pulses, to avoid an overlap between the statistics from consecutive pulses.
- The detector must provide a precise subtraction of the two photocurrents (high subtraction efficiency), in order to eliminate the classical noise of the *LO*. This requirement is easier to satisfy at lower *LO* energies; however, at the same time, the *LO* power must be also high enough to give a sufficiently strong subtraction signal I_{Φ} [19].
- The *shot noise* difference charge must be low-noise amplified and a flat amplification profile must be provided.
- All these characteristics have to be verified in the entire frequency range from DC to at least the *LO* pulse repetition rate (high bandwidth).

Moreover, the previous theoretical treatment of the Balanced Homodyne Detection is not exactly correct in pulsed regime: we considered the *signal* and the *LO* as single mode optical fields generated by the same laser source; in this case, they cannot be monochromatic as they are pulsed. In order to fill this conceptual gap, we developed a mathematical formalism in order to generalize the theoretical treatment of the single-mode Balanced Homodyne Detection also to the pulsed regime (Appendix C).

In a generic *BHD* apparatus, a pair of high-efficiency photodiodes are wired in series to subtract their output currents, this difference signal is then amplified and stored in a digital oscilloscope. The data are numerically integrated over time intervals corresponding to the duration of each pulse; then, one extracts the area of each pulse in the difference signal and performs statistical analysis.

The integral of each pulse in the difference signal is the quantity associated to the field quadrature in a pulsed *BHD* experiment.

The typical problem is that an amplifier with higher bandwidth usually exhibits poorer noise characteristics. So, a tradeoff has to be found between the bandwidth and the signal-to-noise ratio, that, more precisely, is a *shot-to-electronic noise ratio*.

In photodetection, *shot noise* describes the fluctuations of the number of photons detected. In our case it is the fluctuation of the light intensity measured by each photodiode. To be directly measurable it has to dominate the noise of the subsequent electronic amplifier.

It is important to note that the shot noise is not a property of the detector, but it reflects the real fluctuations of the light intensity and we can use the detector itself to probe the statistics of the light fluctuations. This will be correct as long as the efficiency of the detector η_{det} approach 1.

For $\eta_{det} = 1$ the photocurrent fluctuations are directly linked to those of the light and we can investigate the statistical properties of the light studying the current fluctuations.

To check that the pulsed noise $\Delta I_\Phi = \langle (I_\Phi - \langle I_\Phi \rangle)^2 \rangle$ generated by the homodyne detector with a vacuum *signal* in input is indeed the shot noise, one needs to verify that the noise variance (ΔI_Φ) scales linearly as the *LO* power increases. This is a signature distinguishing the *shot noise* from the *classical noise*, which scales quadratically, and the *electronic noise*, which is constant because independent from the *LO* intensity [20].

2.5 State of art

The first time-domain *BHD* experiment, performed by Smithey et al. in 1993 [2], achieved a shot-to-electronic noise ratio of 9 dB and worked at a repetition rate of 1 kHz. It is a relatively low frequencies compared to the repetition rate of the commonly used pump mode-locked laser.

The use of low-repetition-rate laser source, in the first *BHD* experiments, was forced because of the dead time of the low-noise charge amplifiers, which provided a maximum pulse acquisition rate well below the MHz.

Hansen and colleagues in 2001 [21] built a *BHD* working at a repetition rate of 1 MHz with a shot-to-electronic noise of 14 dB.

However, in order to access quantum states with a low generation probability,

a time-domain homodyne detection capable to work at the high repetition rate of mode-locked lasers (tent of MHz) is required.

So far, only few groups in the world were able to obtain this goal (for example [22, 23, 24]). In particular, Zavatta at al. reached this aim for the first time [25], developing an homodyne detector working at a repetition rate of 82 MHz with a shot-to-electronic-noise ratio of 7 dB.

The aim of this thesis is to implement a *BHD* apparatus in time-domain regime with a mode-locked laser source. In our apparatus we don't use an electronic scheme built *ad hoc*, as it happens in the just cited papers, but a commercial device for the homodyne photocurrent detection is exploited. To our knowledge, there is no published paper about pulsed balanced homodyne detection apparatus implemented with a commercial differential photodetector.

Chapter 3

Experimental apparatus

The implementation of a balanced homodyne detection apparatus for time domain quantum tomography of pulsed optical quantum states must comply with the following experimental requirements.

- In order to measure field quadratures with temporal resolution sufficient to distinguish between consecutive pulses of the laser source, a **high bandwidth** detection system is required. It should be noted that a high bandwidth low noise amplified detection system is technically challenging as increasing the bandwidth implies reducing the amplification gain and therefore increasing the electronic noise.
- The detection apparatus must also ensure a high ratio of the measured quantum noise over the electronic noise, that means a sufficiently **high shot-to-electronic noise ratio**.
- Another key point of the apparatus is the ability to efficiently perform the difference between the amplitude fluctuations of the beams impinging on the two detectors, reaching a **high subtraction efficiency** between the two photocurrents generated by the photodiodes. This is expressed by the Common Mode Rejection Ratio (*CMRR*), defined as the spectral power measured when both photodiodes are illuminated divided the power measured on one photodiode when the other is blocked. The *CMRR* measures the ability of the device to reject the classical noise of the local oscillator [26].

- Finally the two photodiodes must have the same **high quantum efficiency** (ideally $\eta_{det} \sim 1$). This is a fundamental condition in order to actually measure the *signal* noise statistic [11]. Small differences in the quantum efficiencies of the two photodiodes can be compensated using half wave plates and polarizers as variable attenuators of the input of each photodiode.

In this chapter we describe the instrumentation used to implement our balanced homodyne detector in pulsed regime; in the next chapter we will characterize all the parts constituting it, in order to satisfy the previous experimental requirements.

The apparatus is divided in three parts: the laser source, the optomechanical scheme and the acquisition system.

3.1 Pulsed laser source

The light source in our homodyne detector is a mode-locked pulsed laser. Mode-locking is a technique by which a laser can be constructed to produce pulses of light of extremely short duration. This kind of ultrafast laser systems are capable of producing a train of ultrashort pulses, with a temporal duration of 100 – 1000 fs and an extremely high *repetition rate* (number of pulses per unit of time, measured in Hz).

In particular, our laser source is a Kerr lens mode-locked Ti:Sapphire oscillator (*Mira Seed*), in which the active medium is Ti doped Al_2O_3 .

This source is pumped by a solid state laser which produces 18 W of monochromatic continuous wave radiation at 532 nm (*Verdi V-18*).

The final laser output consists of a train of 100 fs pulses with a fixed repetition rate of 80 MHz. The pulse photon energy is 1,55 eV (i.e. a wavelength of 800 nm) and it is called the fundamental of the laser.

The oscillator has an output average power of 800 mW, of which only few mW are used for our experiment. The laser power fraction needed in our experiment (4 – 5%) is taken using an unbalanced beam splitter placed at the laser source output. The remaining fraction, which is the most part of the laser source, goes in a regenerative amplifier system (*REGA*) and in an optical

parametric amplifier (*OPA*), to be finally used as a source for experiments of ultrafast spectroscopy, which is the research field mostly developed in the laboratory in which this thesis has been carried out. We will not discuss the amplification system which has not been used in the experiment.

A block representation of the laser system used in our experiment is given in Figure 3.1.

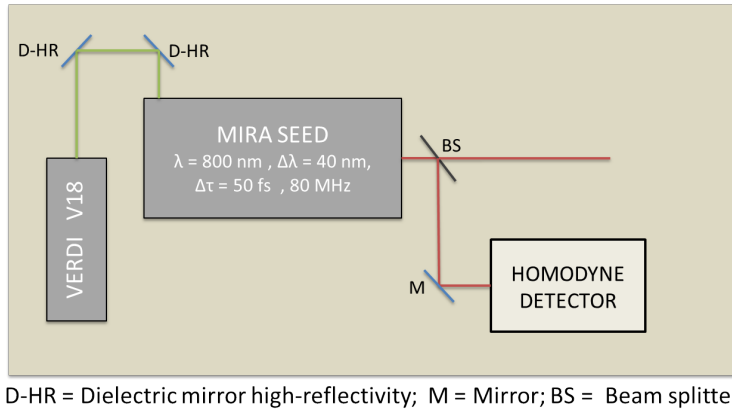


Figure 3.1: Block diagram of the laser system.

The production of short laser pulses in Ti:Sapphire laser is based on the concept of mode-locking. In a laser cavity sustaining many longitudinal modes, a pulsed regime can be reached when all the modes participating to the lasing can be *locked* in phase, i.e. a fixed phase relation between them is induced.

In the next section we will see in detail the most common passive scheme to obtain mode-locking, Kerr Lens mode-locking (*KLML*). The *KLML* technique exploits non linear optical proprieties of the active medium together with the geometrical structure of the laser cavity to generate ultrashort pulses.

For a detailed quantum mechanical treatment of mode locked laser pulses see Appendix C.

3.1.1 Kerr lens mode-locking

The electric field in a laser cavity is made up of the sum of all the *longitudinal modes* of the cavity. Their wavelengths have to verify the relation $L = l \frac{\lambda}{2}$, where L is the cavity length and l are integers known as *mode orders*.

The frequency separation between two consecutive modes is $\Delta\nu = \frac{c}{2L}$ where c is the speed of light.

In a simple laser, the longitudinal modes oscillate incoherently, i.e. with random phase relationships between each other. This leads to random fluctuations in the laser output intensity with periodicity $\tau = 1/\Delta\nu$ (Figure 3.2 b). When the longitudinal modes are many thousands, the interference effects between them tend to average to a near-constant output intensity and the laser emission is called continuous wave (CW).

Mode-locking consists in forcing each longitudinal mode to have a fixed phase relation with the others, in this way the modes of the laser will all constructively interfere, producing, instead of a random or constant output intensity, a train of light pulses separated in time by $\tau = \frac{2L}{c}$.

For example, if the phase difference between two consecutive modes is forced to be constant ($\varphi_{l+1} - \varphi_l = \varphi_0$), the total electric field in the laser cavity is:

$$E(t) = \sum_{l=-M}^M E_0 e^{i[\omega_l t + \varphi_l]}, \quad (3.1)$$

where we assumed for simplicity the same amplitude E_0 for each mode, $\omega_l = \omega_0 + l\Delta\omega = 2\pi(\nu_0 + l\Delta\nu)$ is the l_{th} mode frequency and $\varphi_l = l\varphi_0$ is the mode-locked phase.

The total number of longitudinal modes in the cavity is $(2M + 1)$.

Separating in two part the sum in the (3.1) and using the geometric series convergence, it's easy to show that:

$$E(t) = E_0 \frac{\sin\left(\frac{2M+1}{M}t'\right)}{\sin\left(\frac{1}{2}t'\right)} e^{i\omega_0 t}, \quad (3.2)$$

where $t' = \Delta\omega t + \varphi_0$.

A plot of the intensity of such electric field in time domain is given in the Figure 3.2 c, for the case of locked phases.

It is possible to observe that the pulse intensity is proportional to $[(2M + 1)E_0]^2$, the pulse full width at half maximum (FWHM) is $\frac{2\pi}{(2M+1)\Delta\omega}$ and the distance between two pulses is $\tau = 2\pi/\Delta\omega$.

The ratio between the laser cavity length L and the pulse duration is a measurement of the number of modes oscillating in phase. Typically, for a meter long laser producing a train of 100 fs pulses, there are over 10^4 modes

contributing to the pulse bandwidth.

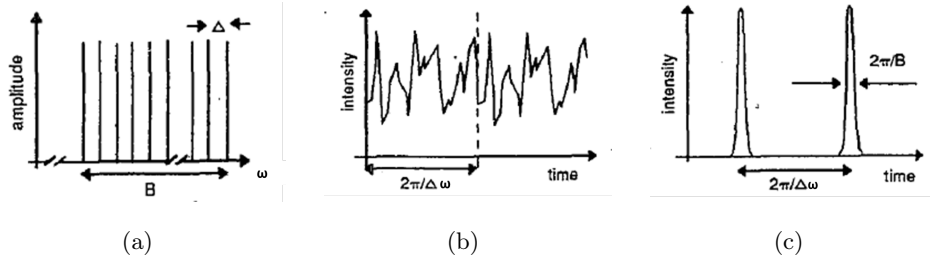


Figure 3.2: Set of equally spaced longitudinal modes ($B = (2M + 1) \Delta\omega$) (a). Inverse Fourier transform of the laser spectrum in case of random phase distribution of the modes(b), and in case of *locked* modes(c) [27].

Several techniques to lock the longitudinal modes in a laser cavity exist.

The Kerr lens mode-locking method exploits a nonlinear optical process known as the *optical Kerr effect (OKE)*. It is based on the dependence of the refractive index of a medium on the electromagnetic field intensity, i.e. the fact that non linear terms contribute to the medium refractive index when the incident field is sufficiently intense.

Since the light beam in a laser cavity has a transversal Gaussian power density distribution, the refractive index changes across the beam profile. The beam experiences a refractive index greater in its center than at the edge [28].

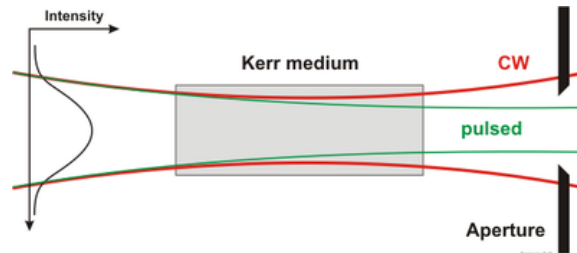


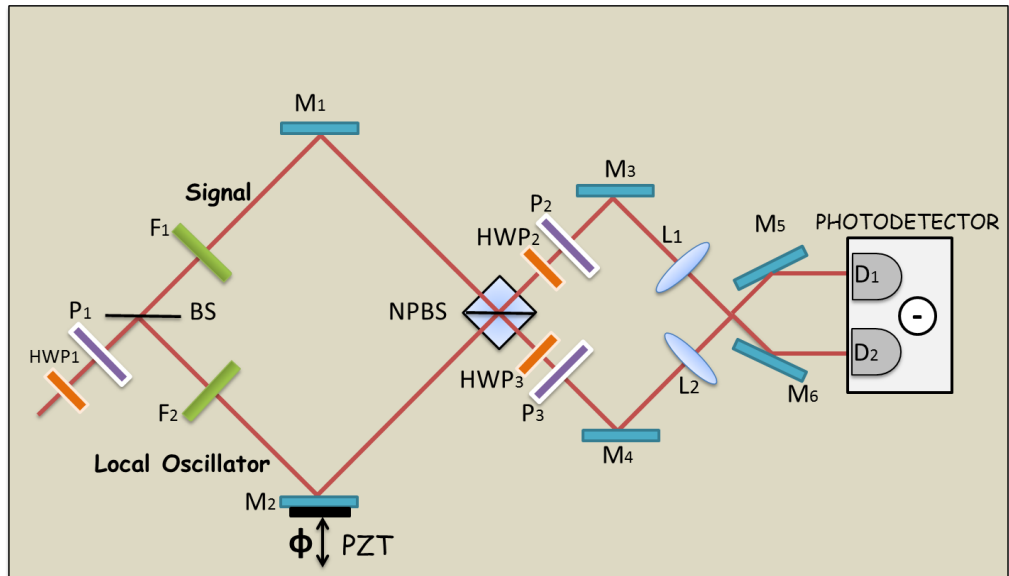
Figure 3.3: Kerr lens scheme [29].

In this way the active Kerr medium works like a lens and focuses the beam. Since this effect is proportional to the field intensity, in the laser cavity this “focalization” will be different for pulsed and continuous wave mode. The geometrical properties of the cavity and of its aperture play at this point an important rule, they are designed to favor operation of pulsed over

continuous radiation due to intensity dependent loss or dispersion mechanisms. When such conditions are fulfilled, intensity fluctuation will be amplified, continuous wave lasing modes will be suppressed and the cavity will "lase" in the pulsed regime. The end mirror of the cavity will then partially transmit the pulses sustained by the cavity and a train of pulses at the repetition rate of $(\tau)^{-1} = \frac{c}{2L}$ will propagate in the free space.

3.2 Optomechanical scheme

The core of the homodyne detector is a Mach-Zehnder interferometer. A scheme of the optomechanical system is given in Figure (3.4).



HWP=Half Wave Plate; P=Polarizer; M=Mirror; F=Neutral filter; PZT=Piezoelectric translator; NPBS=Non polarizing beam splitter; L=Lens; D=Photodiode

Figure 3.4: Optomechanical scheme

The laser source is divided in two beams by a beam splitter, one is the so called *local oscillator* (*LO*) and the other, made weaker by a reflective neutral density (ND) filter (F_1), is called *signal* and is the field we want to investigate. The *signal* power can be made even weaker by using filters with higher optical densities. In order to make equal the optical paths of the two beams, an other neutral-density filter (F_2), of optical density $OD = 0.2$, is placed on

the local oscillator arm too. The optical density of a filter indicates that the attenuation factor of the input beam is 10^{-OD} .

The two beams interfere in a second beam splitter and the output beams are detected and subtracted by a commercial photodetector.

Two 100 mm lenses focus the output beams onto the entrances of the photodetector. In Figure 3.5 a picture of the experimental optomechanical set up is shown.

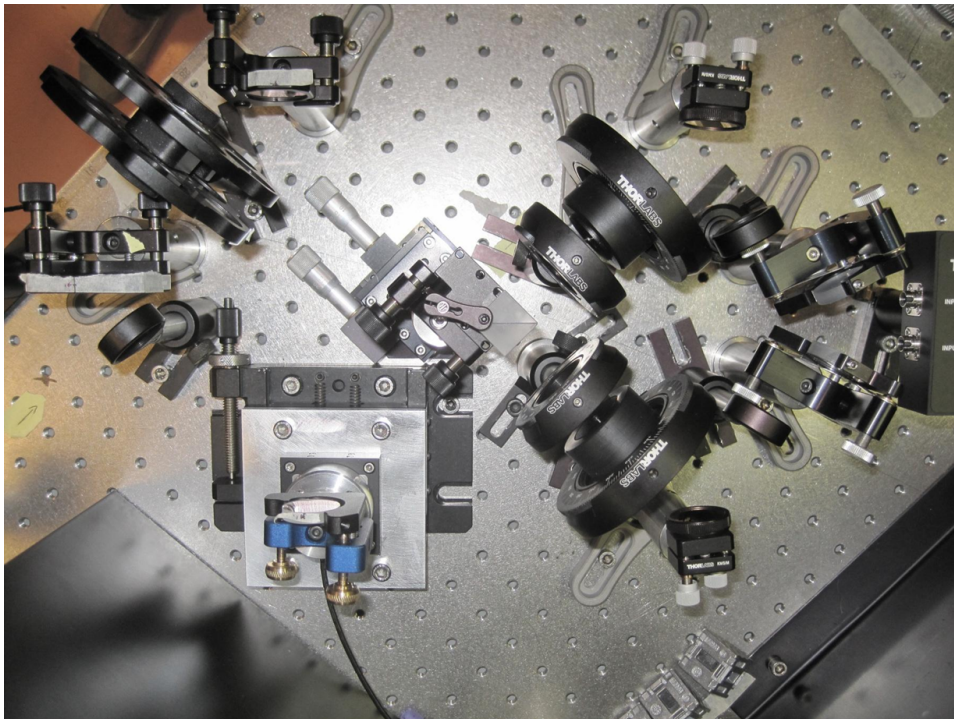


Figure 3.5: Experimental optomechanical set up

The phase difference Φ between the two arms of the interferometer can be varied by moving a mirror set up on a piezoelectric translator in the LO arm. The piezoelectric translator is a piezo linear stage (*PI P622-ZCD*) with a travel range of $250\ \mu\text{m}$ and a $1\ \text{nm}$ nominal resolution. The stage position is controlled by a Piezo Servo-Controller (*PI E625*). The latter is equipped with a RS-232 interface connected with a computer.

A software has been developed, using the programming language LabVIEW, to control and to read the piezo stage position along the motion axis.

The total laser power can be varied by means of a half wave plate followed by a polarizer at the beginning of the system.

Other two pairs of half wave plates and polarizers are put at the outputs of the second beam splitter, which is a (50/50) non polarizing cube beam splitter (NPBS). In this case, they are used to compensate the different efficiency of the photodiodes in the differential detector. In the experiment they are used to minimize the difference current measured by the differential photodetector when the *signal* is blocked.

3.3 Acquisition system

A scheme of the acquisition system is given in Figure 3.6.

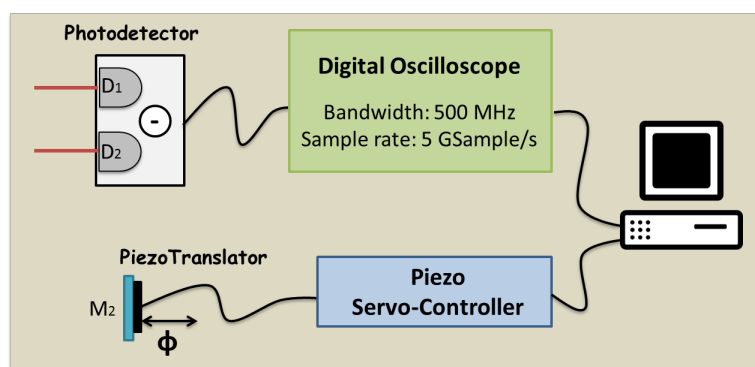


Figure 3.6: Block diagram of the acquisition system

It consists of a balanced amplified differential photodetector (*Thorlabs PDB430A*) which is able to measure the difference between the photocurrents generated by the two beams in input.

We chose this commercial device for its characteristic of **high bandwidth** (from DC to 350 MHz) , **high subtraction efficiency** and **high photodiodes quantum efficiency**.

It consists of two *Si*/PIN well matched photodiodes and an ultra-low noise, high-speed transimpedance amplifier that generates an output voltage proportional to the difference between the photocurrents of the two photodiodes, i.e. the two optical input signals. The two diodes have nominal values of the quantum efficiency of 0.77. The photodetector has a nominal value of the

$CMRR > 25\text{ dB}$. The damage threshold of the input power for each diode is 20 mW .

The photodetector output signal (difference signal) is recorded by a digital oscilloscope (*Tektronix TDS3000B*) with a bandwidth of 500 MHz and a sampling rate of 5 Gsamples/s, this means we can digitize the voltage output of the differential detector with a sampling rate of a point every 0.2 ns. The oscilloscope traces are finally sent to a computer to be memorized and analyzed.

3.3.1 Acquisition software

In order to perform quadrature measurements of the field under investigation through our homodyne detection apparatus in pulsed regime, a series of softwares have been developed, using the programming language "LabVIEW". Such softwares allow us to control the piezomotor, deciding the number and the length of the piezo steps to do in a measurement, and, for each position, to digitalize and memorize a well-defined number of oscilloscope traces.

In addition to the possibility of choosing the number of traces per position to acquire, one can also set the number of pulses for each trace. Then the software provides the integral of each pulse in the acquired trace and the corresponding read piezo position.

In this section a schematic description of the acquisition software working is given:

- Initial settings : number of piezoelectric positions, step length, number of traces per position, number of pulses per trace.
- The piezo-translator moves and for each position the following operations are performed:
 - Acquire and save the oscilloscope trace
 - Read and memorize the piezo position
 - Integrate each pulse in the acquired trace
- Final output: a piezo position and a quadrature value are associated to each acquired pulse

The details of the data analysis are given in the next chapter.

Chapter 4

Pulsed homodyne detector characterization

In this chapter the characterization measurements of the experimental apparatus are described. They are divided in two groups: stability measurements of the optomechanics and characterization measurements of the acquisition system. The aim of all those preliminary measurements is to completely determine the balanced homodyne detector performances in pulsed regime.

4.1 Characterization of the mechanical stability

In order to verify the mechanical stability of the Mach-Zehender interferometer, which is the core of the optomechanical system, two kinds of tests have been done. In the first, we measure the stability of the piezoelectric read-out position, in order to check the piezoelectric translator performances. In the second, we verify the stability and the alignment of the whole optomechanical system using a continuous wave (CW) laser source in input.

The experimental procedures are now described.

4.1.1 Stability of the the piezoelectric read-out position

The piezoelectric translator stage is put at certain position sending a specific command to the Piezo-Servo Controller. In this test the chosen position is $p = 81\mu m$.

Now we use the Controller to read the piezo position for 4000 consecutive times. The read-out values are registered. The mean value and the root mean square are computed.

We obtain $p_{mean} = 81.036$ and a standard deviation of 3 nm .

The histogram of the piezo positions with subtracted mean value is shown in Figure (4.1). The stability in the read piezo position is necessary to associate

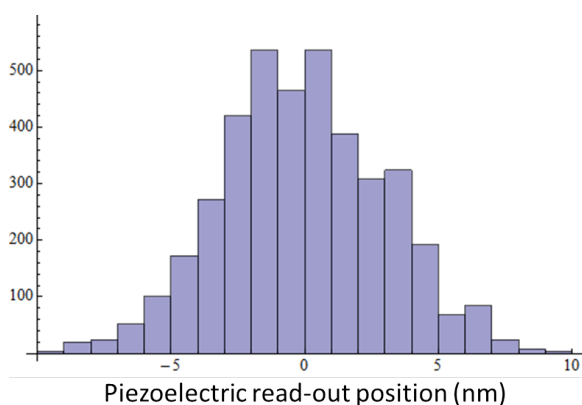


Figure 4.1: Histogram of 4000 read-out piezo position subtracted of the mean value.

the right phase value Φ to a certain measured quadrature x_{Φ} in the homodyne detection.

Our apparatus allow us to read the piezo position with an error of $\pm 3\text{ nm}$.

4.1.2 Interferometer stability measurement with CW laser source

In order to check the interferometer stability performance we use a *CW* laser source. It is a He-Ne laser pointer with wavelength $\lambda = 632.8\text{ nm}$.

In this case the filters in the two interferometer arms (Figure 3.4) are removed, in order to have the same intensity for the *LO* and the *signal*.

The piezoelectric translator is moved of 50 nm for 100 steps. At each position 100 traces of the difference signal measured by the photodetector are acquired by the oscilloscope (Figure 4.2). The sum of all the voltages divided by the number of traces is plotted against the piezo position (Figure 4.3). Given the piezo shift d between two peaks of the interference figure, the actual optical

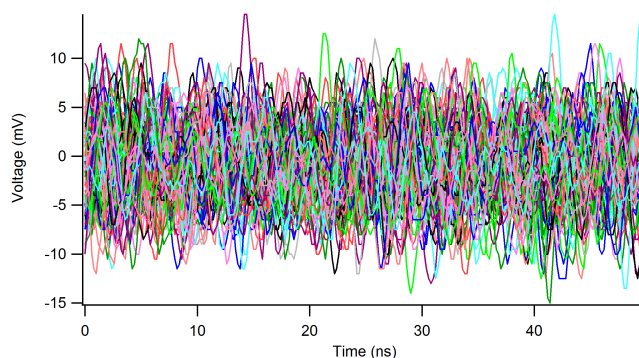


Figure 4.2: 100 difference signal traces acquired by the oscilloscope. CW laser source.

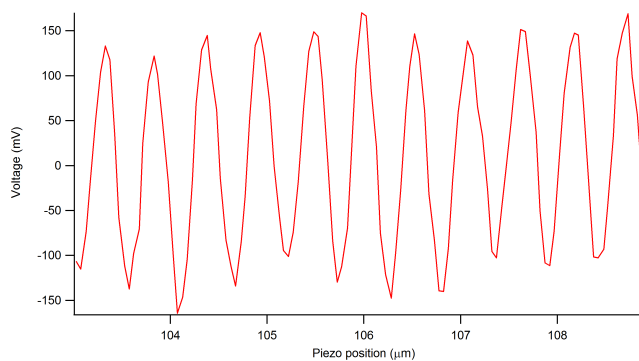


Figure 4.3: Difference signal against piezoelectric translator position. CW laser source.

path difference between the two beams is $D = \sqrt{2}d$, due to the geometry of the apparatus.

If the interferometer works correctly, the optical path difference D between the two peaks of the interference figure should be equal to the wavelength λ of the CW laser source. Our measurement (Figure 4.3) verifies such condition.

4.2 Characterization of the differential acquisition system

After the first check of the interferometer stability with a CW laser source, we performed a series of measurements to characterize the apparatus for the

acquisition in pulsed regime, that is when the mode-locked oscillator is used as source.

The characterization of the differential detector in pulsed regime is performed in the experimental configuration described in Figure 3.4, where the *signal* beam is closed by a beam blocker (vacuum state in input).

In this section the experimental details of these preliminary measurements are presented.

4.2.1 Acquisition in pulsed regime

When the pulsed laser source is used, the local oscillator power can be controlled changing the orientation of a half wave plate (HWP_1 in Figure 3.4). The LO power can be tuned in the range from $90 \mu W$ to $890 \mu W$. This power is measured using a power-meter with sensitivity of $5 \mu W$. The following tests are performed at the maximum LO power.

In this configuration, for a fixed position of the piezo translator, a time-trace of the difference signal measured by the detector is acquired. The oscilloscope is configured to acquire 250 points for each trace, since it takes a point every 0.2 ns (5 Gsample/s sampling rate), every trace contains 4 pulses. Since the pulse width is much shorter than the time resolution of the electronics, the shape of the acquired pulses is given by the detector response function.

The acquisition is done at first by closing one by one the photodiodes entrances and afterwards keeping both open, in order to see a trace of positive pulses, negative pulses, and the difference of the two (Figure 4.4). // The difference signal (green curve in Figure 4.4) is not exactly zero, there is indeed a residual shape in the pulsed regions due to the different response functions of the two photodiodes in the detector.

This shape of the difference signal can be balanced by slightly changing the orientations of the half wave plates placed after the BS (Figure 3.4).

To quantify the subtraction efficiency in the chosen configuration, we estimate the Common Mode Rejection Ratio ($CMRR$). This is a measure of the subtraction ability of the differential detector.

The detector output could be ideally expressed as $I = A(I_1 - I_2)$, where I_1

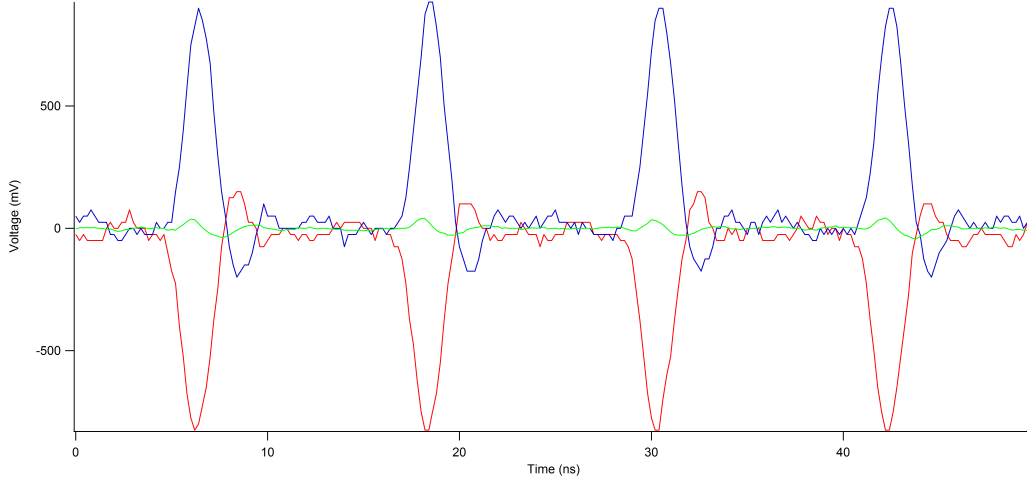


Figure 4.4: Time-traces of 4 individual pulses. The red and blue traces are detected closing the photodiodes entrances one by one; the difference signal is acquired when both photodiodes are illuminated. LO power: $890 \mu W$

and I_2 are the input signals. However, for a real differential photodetector, the output I_0 is described as [26, 30]:

$$I_0 = A_1(I_1 - I_2) + \frac{A_2}{2}(I_1 + I_2) \quad (4.1)$$

where A_1 is the rejection mode gain and A_2 is the common mode gain.

When I_0 , I_1 and I_2 are represented in powers, the $CMRR$ is defined as:

$$CMRR = 10 \log_{10} \left| \frac{A_1}{A_2} \right|. \quad (4.2)$$

To estimate this quantity experimentally, the following approximations are used:

- When only one photodiode is illuminated and the other is blocked ($I_2 = 0$), the output is

$$I_{0a} = A_1 I_1 + \frac{A_2}{2} I_1 \approx A_1 I_1 \quad (4.3)$$

Such approximation is valid because for a balanced differential detector the rejection mode gain is far larger than the common mode gain ($A_1 \gg A_2$).

- When both photodiodes are illuminated, assuming the input signals are perfectly balanced (i.e. $I_1 = I_2$), the output is

$$I_{0b} = A_1(I_1 - I_2) + \frac{A_2}{2}(I_1 + I_2) \approx \frac{A_2}{2} 2I_1 = A_2I_1 \quad (4.4)$$

Under these approximations $\frac{A_1}{A_2} \approx \frac{I_{0a}}{I_{0b}}$.

Thus, the *CMRR* can be calculated from the ratio between the spectral power measured when both photodiodes are illuminated (I_{0a}) and the power measured when one photodiode is blocked (I_{0b}). In our case, $I_{0a} = (6.575V)^2$ and $I_{0b} = (105mV)^2$. The numeric values in such expressions are given integrating the voltages in Figure (4.4) (blue and green curves) in the pulse region¹.

The *CMRR* estimation in our configuration is $10 \log_{10} \left| \frac{I_1}{I_2} \right| = 36 \text{ dB}$. This is in agreement with our detector specifications, described in Section 3.3.

Greater subtraction efficiencies could be obtained with a differential photodetector built "ad hoc" [25, 22, 23].

4.2.2 Photodetector linearity test

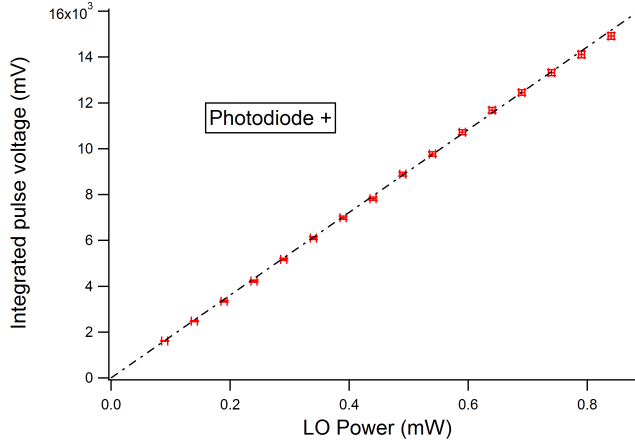
The first characterization of the balanced differential photodetector used in the experiment concerns the characterization of the two photodiodes independently. In order to test the linearity of each photodiode we proceed as follows: we keep the photodiodes open one at a time and we measure the output voltage as a function of the *LO* intensity, which can be controlled by the HPW_1 in Figure (3.4). The *signal* beam is blocked.

In each measurement set the output voltage over the pulse region is integrated for 1000 different pulses. The average value of these integrals is plotted for both photodiodes as a function of the *LO* power (Figure 4.5).

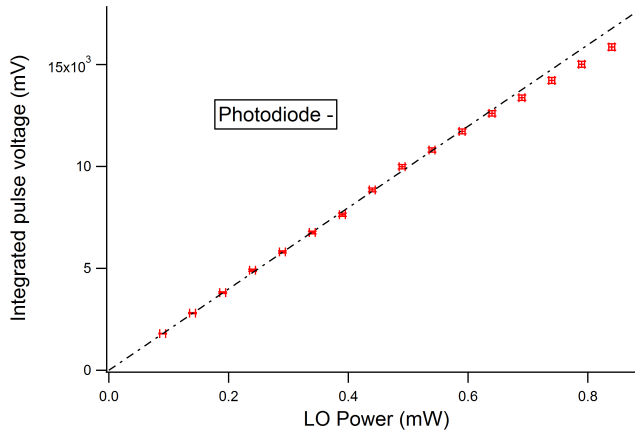
In Figure 4.5 a linear fit to the data is reported.

It's possible to note that the response of the diodes is linear up to 0.6 mW *LO* power, while it becomes non-linear for higher fluencies.

¹The right expression for I_{0a} and I_{0b} in terms of powers can be obtained dividing them by the termination resistance of the oscilloscope ($R = 50\Omega$); we neglected this factor since it is not relevant in the ratio of the two quantities.



(a)



(b)

Figure 4.5: Mean value of 1000 integrated pulses versus LO power. Photodiode + (a). Photodiode - (b)

These non-linearity effects could be attributed to the photodiodes themselves or to the electronic amplifier in our commercial photodetector device.

4.2.3 Shot noise linearity test

Another important test to study the differential detector performances in time-domain is to measure the *noise variance* as the LO power changes. This is done with the vacuum state in input i.e. *signal* beam blocked.

The noise variance of a balanced differential detector in the shot noise regime

is expected to change linearly in the LO power with a constant offset representing the electronic noise [20].

As described in Section 2.4, the linearity in the noise variance ensures the fact that the measured noise is actually the shot noise.

The procedure used to measure the differential detector noise variance is now presented.

From now on we use the term *time-trace* to indicate the difference signal trace, that is the trace acquired when both the photodiodes entrances are open (for example the green curve in Figure 4.4; Such time-traces contain a series of *pulses* resulting from the subtraction between the photo-currents produced by a pair of light pulses impinging on the photodiodes.

A set of 2000 time-traces, each containing 4 pulses, is acquired for a fixed piezo position (Figure 4.6 a). Thus we have a total of 8000 acquired pulses A_i . The characteristic shape of these pulses, as described before, is due to the different electronic response of the two photodiodes.

The average trace is calculated (Figure 4.6 b) and subtracted from each original trace.

The traces obtained by this procedure are shown in Figure 4.6 c.

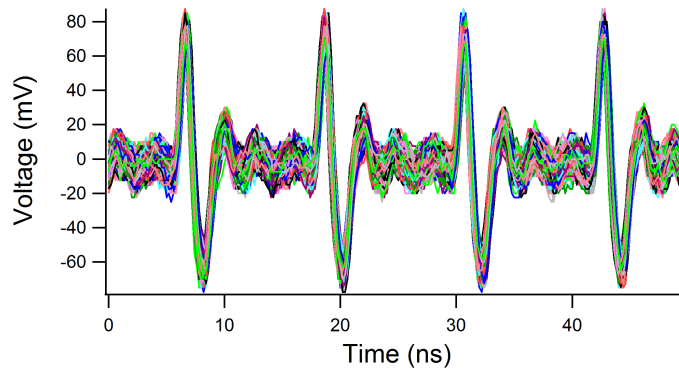
With this procedure, from each original pulse A_i (Figure 4.6 a) we obtain a processed pulse B_i (Figure 4.6 c).

Then, for each processed pulse B_i , the noise N_i is obtained by measuring the integral in the pulse region (integration length 5 ns).

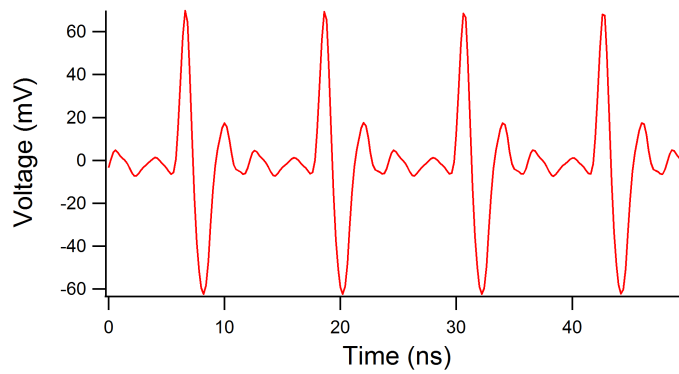
These noise values N_i are the quantities which, appositely rescaled, will constitute a measurement of the field quadrature. In this particular case (*signal* beam closed in Figure 3.4) the field under investigation is in the vacuum state.

Finally, the variance of the quantities N_i is calculated, this is the **HD noise variance** of our apparatus.

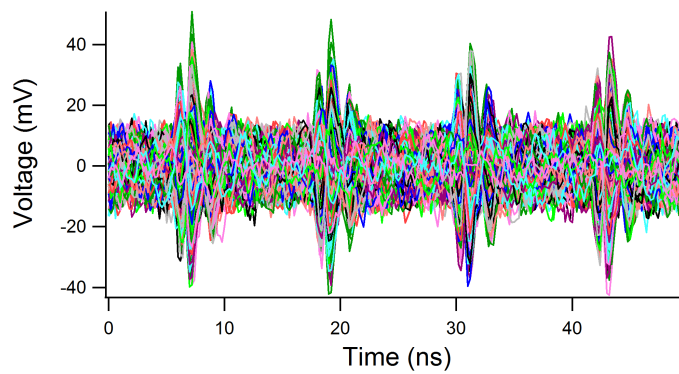
In order to have a characterization of the *HD* noise, the procedure is repeated for different values of the LO power. In Figure 4.7 the HD noise variance values are plotted as a function of the LO power. In Figure 4.7 it is possible to note an expected electronic noise background and a linear regime of the HD noise variance up to 0.6-0.7 mW LO power.



(a)



(b)



(c)

Figure 4.6: Data processing procedure, LO power 0,6 mW. (a) 2000 original time-traces (8000 pulses A_i). (b) Average trace. (c) 2000 processed traces (8000 processed pulses B_i)

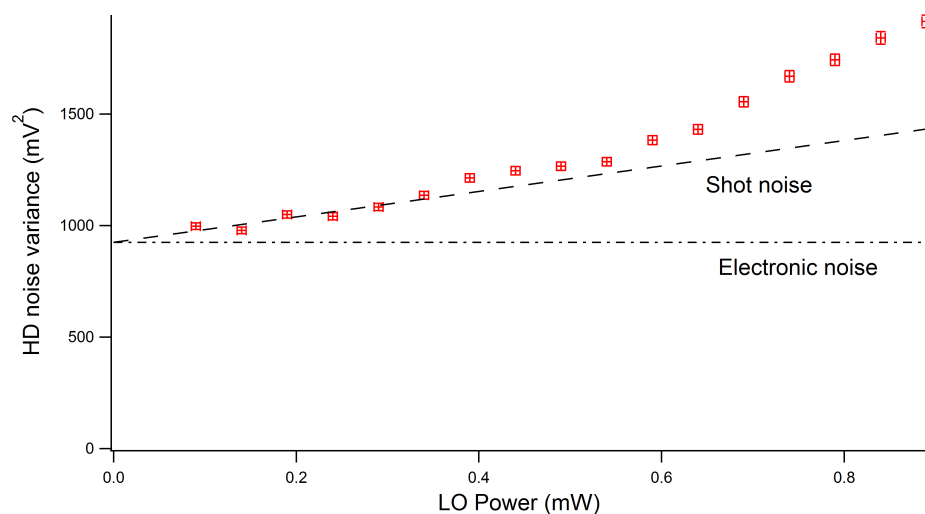


Figure 4.7: HD noise variance versus local oscillator power. Dashed curve, shot noise contribution; dashed-dotted curve, electronic noise background.

It is easy to note that the data deviate from linearity just in correspondence to the beginning of the non-linearity observed in the characterization of the photodiodes (Figure 4.5).

The coincidence between the deviation from linearity of the photodetector response and the onset of non-linear noise is likely not coincidental. When the non-linearity of the photodetector amplifier sets in, a high electronic noise is observed.

The conditions of the photodetector linearity and of the HD noise variance linearity define the optimum LO power to be used in the homodyne measurements.

We chose to work at 0.6 mW LO oscillator power. This is the maximum power at which the HD noise variance is linear, so at this power there is the maximum **shot-to-electronic noise ratio** ($S = 1.2$) achievable in the linear regime of our balanced detector.

The electronic noise is due to any non-desiderable ambient noise, dark current noise from the photodiodes and the intrinsic noise of the amplifier in the differential photodetector.

In our apparatus the electronic noise constitutes a significant contribution to the shot noise.

The electronic noise effect is to add a random quantity to each field quadrature measurement. It was demonstrated [31] that this effect is equivalent to that of optical losses. We will treat this problem in the *Data analysis* chapter (Section 6.2.1).

4.3 Correlation test between successive pulses

In a pulsed balanced homodyne detector it's very important to verify that we are measuring n independent copies of the same state, so that each pulse yields only one quadrature value.

In order to verify this hypothesis we performed a correlation test between two subsequent pulses. In Figure (4.8) a parametric plot of 20000 vacuum

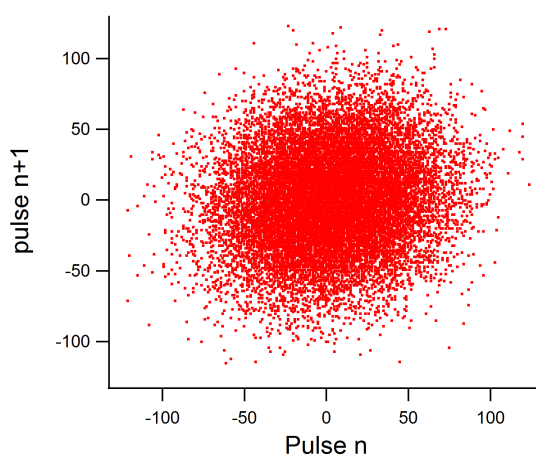


Figure 4.8: Plot of 20000 vacuum integrated pulses. Each integrated pulse ($n + 1$) is plotted against the previous one (n) at a LO power of 0.6 mW.

integrated pulses (the pulse $n + 1$ is plotted against the pulse n) is shown. The lack of correlation in this plot demonstrates that there is no significant impact on the measured integral of the pulse $n + 1$ from that of the pulse n .

We make the analysis more quantitative evaluating the Correlation Coefficient (CC) between adjacent pulses [26]. This is a simple check of the randomness of the noise.

At the chosen LO power, we measure 200 homodyne traces, each containing

10 pulses.

For each pulse we determine the noise N_i as described in the previous section. Now we consider the data arrays $A(k)$ and $B(k)$, each containing 200 noise values, such that:

$$A(k) = N_k, \quad B(k) = N_{k+m}, \quad (m = 0, 1, 2, \dots, 9). \quad (4.5)$$

The CC between pulse n (data array $A(k)$) and $n + m$ (data array $B(k)$) is defined as:

$$CC = \frac{E(AB) - E(A) \cdot E(B)}{\sqrt{[E(A^2) - E^2(A)] \cdot [E(B^2) - E^2(B)]}}, \quad (4.6)$$

where by $E(X)$ we intend the average value of the elements of the array $X(k)$.

10 data sets each containing 200 pulses are used to evaluate the CC between pulse n and $n + m$ ($m = 0, 1, \dots, 9$). The results are shown in Figure (4.9).

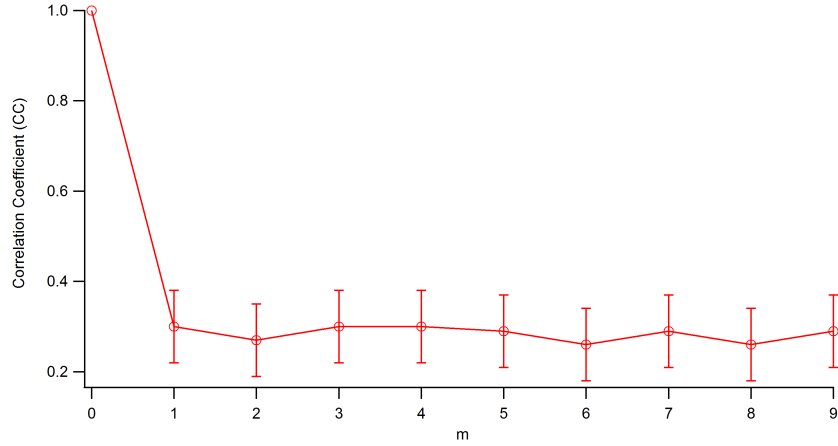


Figure 4.9: CC between different pulses. LO power: 0,6 mW.

The uncertainties in each value are given by the standard deviation of the CC from the 10 data sets.

The CC between pulse n and $n + 1$ is 0.30 ± 0.08 . This value is slightly higher with respect to other reported BHDs [22, 23, 26, 32], in which it always results less than 0.1.

We can conclude that there is a small correlation between adjacent pulses,

but, since the CC has approximately the same value for $m = 2, \dots, 9$, this could be attributed to noise correlation effects at a lower frequency with respect the pulse repetition rate.

Chapter 5

Measurements

After the characterization of the experimental apparatus performances, a set of homodyne measurements for different powers of the *signal* have been performed. The *signal* power in each measurement was controlled by changing the optical density (*OD*) of the filter F_1 in the optomechanical scheme (Figure 3.4). The higher is the *OD* of the filter F_1 , the weaker is the *signal* with respect to the *LO*.

As explained in Section (2.3), we distinguish two homodyne measurement regimes: the *classical regime*, when the *signal* and *LO* are both in a highly excited coherent state and the *quantum regime*, when the *signal* amplitude is much lower than the *LO* one. The conditions for the latter regime are summarized in the equation (2.17).

In this chapter the procedure used to perform homodyne measurements for different *OD* of the filter F_1 is described and the experimental results are shown. In particular, we start from the classical regime and then we progressively attenuate the *signal* (increasing the *OD* of the filter F_1) up to reach the quantum regime. Finally we block the *signal* and we perform a homodyne measurement of the vacuum state.

5.1 Homodyne measurement procedure

In this section we present the procedure adopted to perform a homodyne measurement in a generic configuration. We now consider the configuration

obtained by removing the filters F_1 and F_2 from the optomechanical scheme (Figure 3.4). In this case the LO and the $signal$ have the same power (classical regime). The power value we choose is 0.6 mW (Section 4.2.3).

At first, we need to identify the piezo positions for which the pulses, coming from the two interferometer arms, actually interfere. We move the piezo translator through its entire travel range ($250\text{ }\mu\text{m}$), with steps of 50 nm and at each step we digitalize a homodyne photocurrent time-trace containing 4 pulses, of which we measure the integrals in the pulse regions. The mean value of these integrals is plotted versus the piezo position. The result is shown in Figure 5.1. This kind of measurement gives interferometric autocorrelation

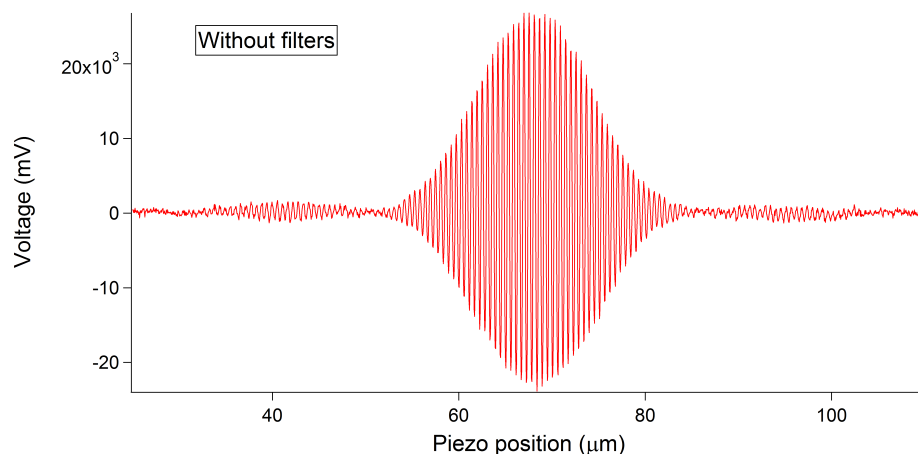


Figure 5.1: Interferometric autocorrelation figure, configuration without filters.

[27] between the pulses and it is commonly used to estimate the duration of ultrashort pulses produced by mode-locked lasers. It should be noted that a linear interferometric autocorrelation gives insights on the real duration of the pulse only in the case those are Fourier-transformed-limited and a non linear technique is necessary otherwise.

We use the interferometric autocorrelation in order to identify the the region of the piezo range for which the pulses interfere. Once such region is identified, we move the piezo translator through a single optical cycle ($1\text{ }\mu\text{m}$) with steps of 5 nm , in correspondence to the center of the interferometric autocorrelation (Figure 5.1). In the considered case the piezo scan is done from $67\text{ }\mu\text{m}$ to

68 μm .

For each step we digitalize 100 time-traces containing 4 difference pulses. For each acquired time-trace we read and save the exact piezo position.

Thus, we measure a total of 80000 difference pulses and their related piezo positions. Each pulse A_i is elaborated and integrated using the procedure described in Section (4.2.3), in order to obtain the noise value N_i . Such values are plotted versus the corresponding piezo positions.

The result, that we called *homodyne trace*, is shown in Figure 5.2. The black solid curve in the figure is obtained by calculating the average of 400 values N_i for each step of the piezo. In the homodyne trace each point is associated

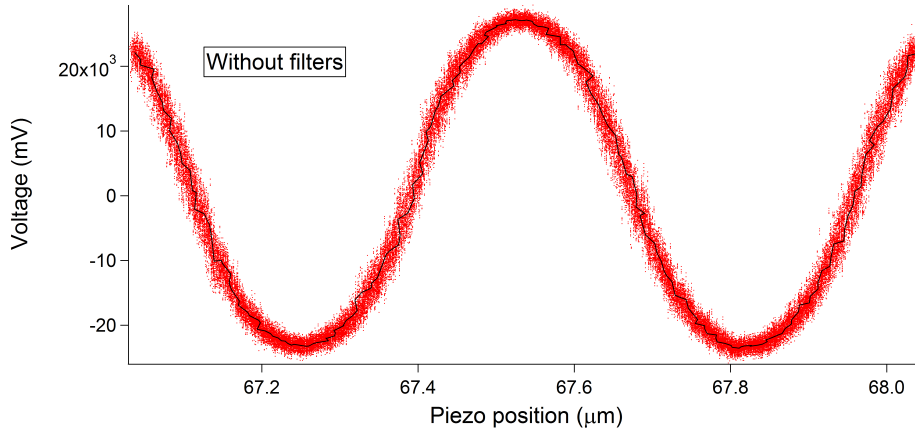


Figure 5.2: Homodyne trace, configuration without filters.

to a pair $(N_i; p_i)$, where N_i is the single difference pulse noise value and p_i is the related piezo position. These quantities, appositely rescaled in the quantum regime, will provide a measurement of the signal field quadrature at a specific phase, that is $(x_\Phi; \Phi)$. The rescaling procedure will be described in the next chapter.

We use the procedure described also for the configurations in which the filters F_1 and F_2 are inserted in the arm of the *signal* and of the *LO* respectively. The piezo position at which we have interference slightly shifts by changing the filter configuration. The small movement (tents of μm) of the interference region observed by changing the *OD* of the filter F_1 is due to the slightly different thickness of reflective filters with different *OD*.

5.2 Measurements in quantum regime

After the first homodyne measurement in the classical regime without filters, we used the configurations in which the filters F_1 and F_2 are inserted in the interferometer arms. In these configurations, for *signal* and *LO* we intend the fields transmitted by the filters F_1 and F_2 respectively (Figure 3.4).

We first achieve a good spatio-temporal overlap (mode-matching) between the *signal* field and the *LO* by carefully adjusting the position of the mirrors and the lengths of the two Mach-Zehnder interferometer arms (Figure 3.4), in order to obtain high visibility interference fringes. Once the visibility is optimized the signal beam is strongly attenuated by means of calibrated neutral density filters (F_1). The optical path length is correspondingly compensated with the filter F_2 . The filter F_1 is different for each measurement because we progressively increases its *OD*. On the contrary, the filter F_2 is the same for all the measurements ($OD = 0.2$), because it has the only aim to match the length of the optical paths in the two interferometer arms (Section 3.2).

Starting from the nominal *OD* of the filter F_1 , we can give a rough estimation of the mean number of photons per pulse in the *signal* field. The procedure used is now presented.

- Using the nominal *OD* of the filter F_1 , we can calculate the power of the *signal* field : $P_s = (0.6 \cdot 10^{-OD}) \text{ mW}$. Where 0.6 mW is the power of the *signal* before going through the filter F_1 , measured by means of a power-meter with $5 \mu\text{W}$ sensitivity.
- We divide P_s by the repetition rate of the laser source (80 MHz) in order to obtain the mean energy per pulse E_{pulse} .
- Since we know the photon energy of our laser source $E_{photon} = 1.55 \text{ eV}$ (Section 3.1), the estimated mean number of photons per pulse will be:

$$n_{est} = \frac{E_{pulse}}{E_{photon}} \approx 0.3 \cdot 10^{(8-OD)}. \quad (5.1)$$

Using the expression (5.1), we can estimate the order of magnitude of the mean number of photons per pulse of the *signal* field, for a generic nominal *OD* value.

We performed a set of homodyne measurements with different OD of the filter F_1 .

The obtained homodyne traces are shown in the following figures.

For each trace we specify the OD of the filter F_1 and the estimated mean number of photons per pulse n_{est} .

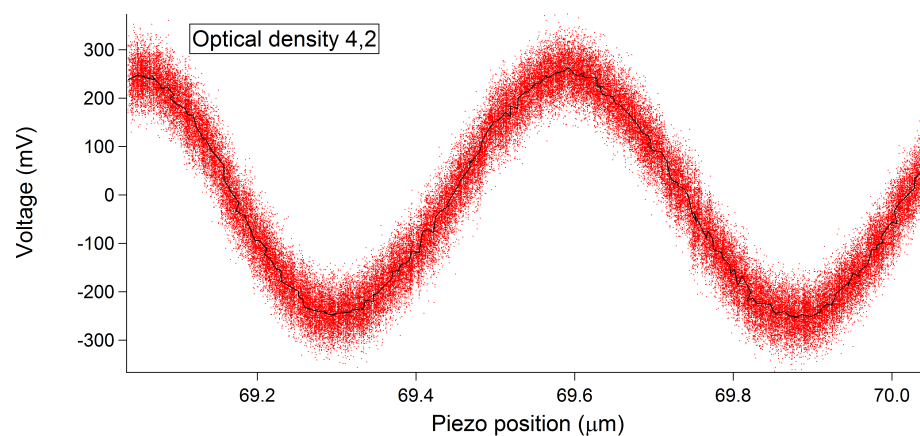


Figure 5.3: Homodyne trace with F_1 $OD = 4.2$; $n_{est} \approx 1.9 \cdot 10^3$.

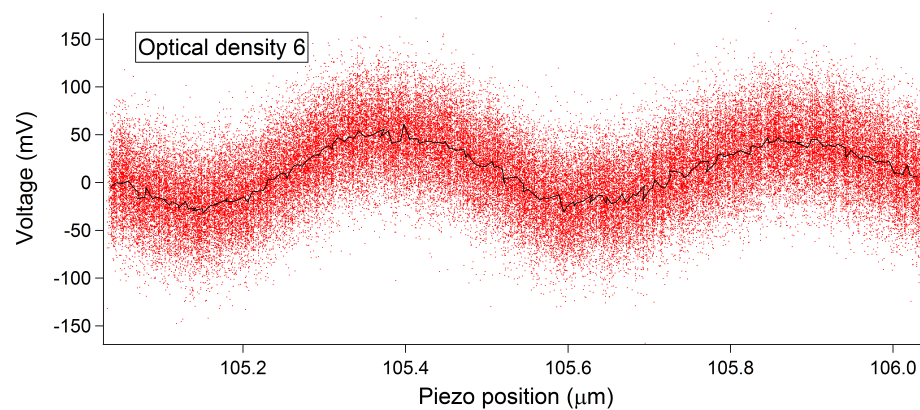
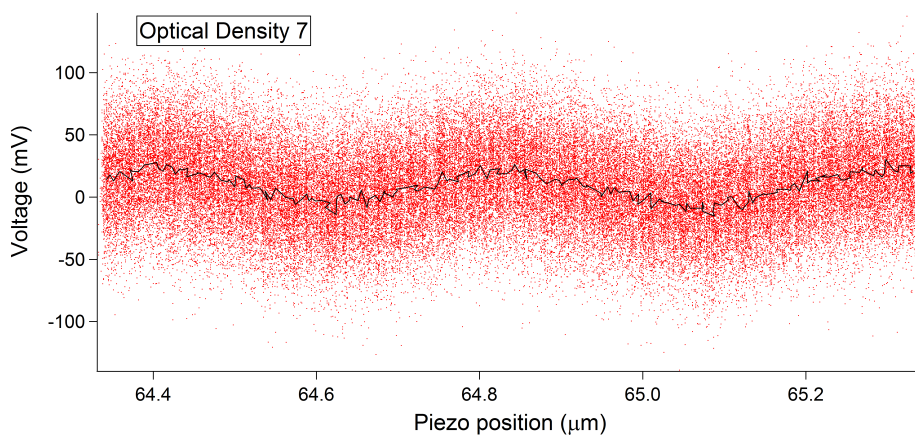
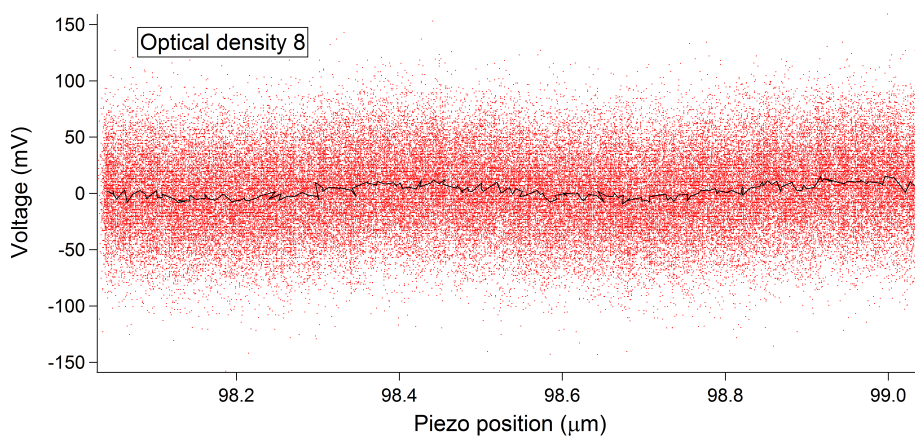


Figure 5.4: Homodyne trace with F_1 $OD = 6$; $n_{est} \approx 30$.

Figure 5.5: Homodyne trace with $F_1 OD = 7$; $n_{est} \approx 3$.Figure 5.6: Homodyne trace with $F_1 OD = 8$; $n_{est} \approx 0.3$.

The modulation of the homodyne noise with the piezo position is due to the coherent *signal* field in input. The amplitude of the *signal* field obviously decreases when the *OD* grows. The modulation is still visible also in the last two cases, where the estimated number of photons per pulse is of the order of unity or lower.

5.2.1 Quadrature measurements of the vacuum state

By closing the *signal* beam with a beam blocker, we perform a homodyne measurement of the vacuum state.

The obtained homodyne trace is shown in Figure 5.7.

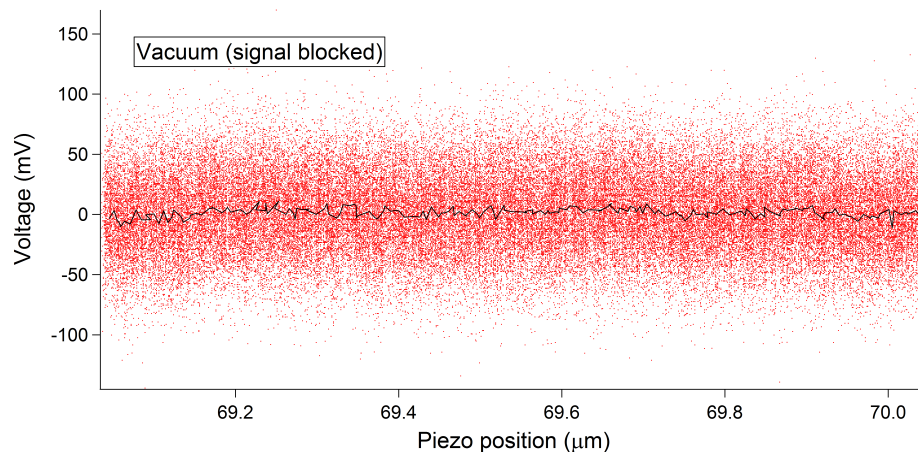


Figure 5.7: Homodyne trace of the vacuum state (*signal* blocked).

As before, the trace is composed of 80000 experimental data N_{i0} and their mean value $\langle N_{i0} \rangle$ results approximately zero as one expects.

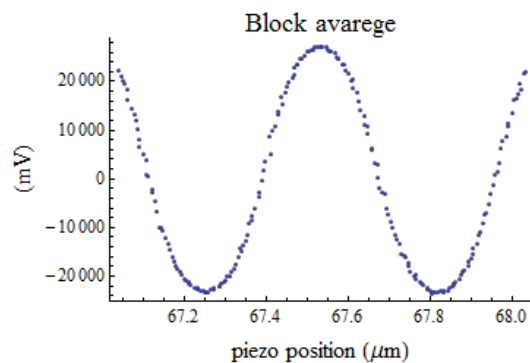
This vacuum homodyne trace will be used as a reference in the next chapter, for the rescaling procedure of the homodyne traces.

5.3 Effects of the piezo translator instability

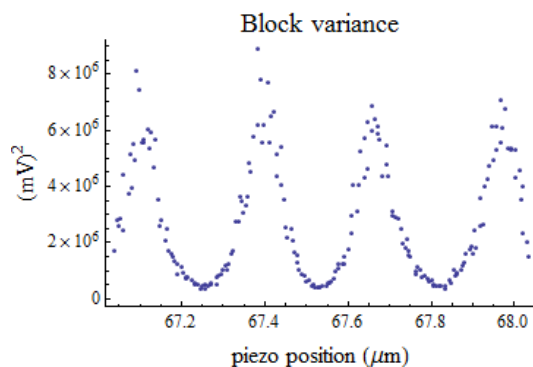
In this section we shall discuss the effect of the the piezo read-out position instability (Section 4.1.1) on the homodyne traces, in particular on the noise variance of the homodyne traces.

We know in advance that our *signal* field is in a coherent state (definition 1.15), because the *signal* and the *LO* are generated from the same pulsed laser source; for this reason the noise variance is expected to be constant as the piezo position changes, both in the classical and in the quantum regime. We show a block average of the homodyne trace in the configuration without filters (Figure 5.8 a); each point is given by the average of a block of 400

noise values in the homodyne trace (Figure 5.2). The block variance is also shown (Figure 5.8 b).



(a)



(b)

Figure 5.8: Block average (a) and block variance (b) of the homodyne trace in Figure 5.2. Configuration without filters. Each block contains 400 data.

It's immediate to note that the variance is not constant as one expects, but it shows a systematic periodicity. The variance is minimum when the derivative of the homodyne trace is minimum and vice versa.

This effect can be attributed to the instability of the read out piezo position (Section 4.1.1). Indeed, an error in the read out piezo position contributes much less to the variance in the regions of minimum derivative than in the other regions of the homodyne trace. Such effect is observable also for the traces in the quantum regime. In that case the modulation of the variance becomes less evident as the OD grows, as one expects.

Chapter 6

Data analysis

In this chapter the procedure used to analyse the measured homodyne traces is presented.

In Section 2.1 we showed that the homodyne photocurrent is proportional to the expectation value of the quadrature \hat{x}_Φ , where Φ is the relative optical phase of the *signal* and the *LO*.

In the following data analysis we rescale the homodyne traces in an appropriate way, so that each point in a trace will be associated to a measurement of the *signal* field quadrature. In other words, each point in a rescaled trace will be given by the pair of measurements $(x_\Phi; \Phi)$.

From a rescaled homodyne trace, we then estimate the expectation value of the number operator on the *signal* coherent state and we compare this one with the mean number of photons per pulse evaluated in the equation (5.1). In addition to this we will show how the low efficiency of the *BHD* can be taken into account.

A series of softwares have been developed, using the programming language "Mathematica", in order to perform the data analysis calculations.

The whole procedure will now be described in detail.

6.1 Rescaling procedure

The homodyne photocurrent in the time-domain regime is integrated for each difference pulse. The obtained value N_i , corresponding to a certain piezo

position p_i , is proportional to the a quadrature value x_Φ :

$$N_i = \gamma' x_\Phi. \quad (6.1)$$

We need to evaluate the proportionality factor γ' in order to obtain the quadrature values from the homodyne trace data.

At this point the homodyne trace of the vacuum state (Section 5.2.1) plays a very important role, since it is used as a reference.

6.1.1 Vacuum analysis

When we block the signal beam in a homodyne measurement, this corresponds to measure the quadrature values of the vacuum state $|0\rangle$.

The quadrature expectation value for the vacuum state is expected to be zero for all phases:

$$\langle \hat{x}_\Phi \rangle_{|0\rangle} = \text{Tr}[\hat{x}_\Phi |0\rangle\langle 0|] = \langle 0 | \frac{(\hat{a}e^{-i\Phi} + \hat{a}^\dagger e^{i\Phi})}{\sqrt{2}} |0\rangle = 0 \quad \forall \Phi, \quad (6.2)$$

while the variance results:

$$\sigma^2[\hat{x}_\Phi]_{|0\rangle} = \langle \hat{x}_\Phi^2 \rangle_{|0\rangle} - \langle \hat{x}_\Phi \rangle_{|0\rangle}^2 = \text{Tr}[\hat{x}_\Phi^2 |0\rangle\langle 0|] = \langle 0 | \frac{\hat{a}^\dagger \hat{a}}{2} |0\rangle = \frac{1}{2} \quad \forall \Phi. \quad (6.3)$$

Thus, we can use the experimental data N_{i0} of the vacuum homodyne trace (Figure 5.7) to evaluate the proportionality factor γ' .

Using the equation 6.1 and imposing the condition 6.3 for the variance of the vacuum state, we obtain:

$$\gamma' = \sqrt{2 \langle N_{i0}^2 \rangle}, \quad (6.4)$$

where $\langle N_{i0}^2 \rangle$ is the variance of the 80000 experimental data in the vacuum homodyne trace (Figure 5.7).

Now, in order to obtain the rescaled vacuum homodyne trace, we divide all these data by the calculated factor γ' (Figure 6.1).

The dotted red lines mark out the root mean square deviation of the rescaled data : $\sqrt{\langle N_{i0}^2 / \gamma' \rangle} = 1/\sqrt{2}$.

In the case of the vacuum, it is not possible to establish the exact relation between the phase Φ and the piezo position because the quadrature is obviously phase-independent.

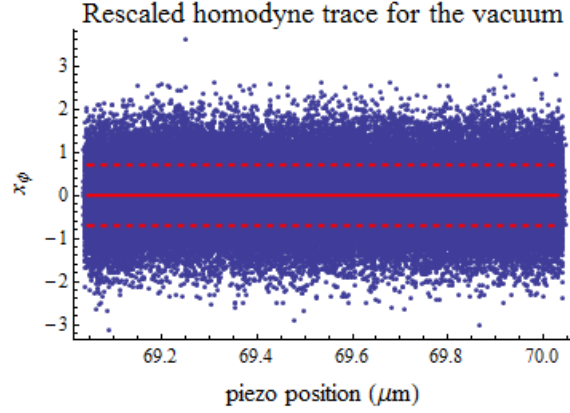


Figure 6.1: Rescaled homodyne trace of the vacuum state (*signal* blocked).

6.1.2 *Signal* analysis

We know in advance that the *signal* under investigation is in a coherent state $|\alpha\rangle$ with $\alpha = |\alpha|e^{i\theta}$.

The field quadrature expectation value for a coherent state is:

$$\langle \hat{x}_\Phi \rangle_{|\alpha\rangle} = \text{Tr}[\hat{x}_\Phi |\alpha\rangle\langle\alpha|] = \langle \alpha | \frac{(\hat{a}e^{-i\Phi} + \hat{a}^\dagger e^{i\Phi})}{\sqrt{2}} | \alpha \rangle = \sqrt{2}|\alpha| \cos(\Phi - \theta), \quad (6.5)$$

where we absorbed θ in Φ .

The quadrature variance results:

$$\sigma^2[\hat{x}_\Phi]_{|\alpha\rangle} = \langle \hat{x}_\Phi^2 \rangle_{|\alpha\rangle} - \langle \hat{x}_\Phi \rangle_{|\alpha\rangle}^2 = \frac{1}{2} \quad \forall \Phi. \quad (6.6)$$

As mentioned before, in order to rescale each pair of data $(N_i; p_i)$ in a homodyne trace in order to obtain the associated pair $(x_\Phi; \Phi)$.

Once the proportionality factor γ' has been calculated using the vacuum trace as reference, we can obtain the value x_Φ from the N_i by dividing this one by γ' ; further, we can find the phase value Φ associated to each piezo position p_i , exploiting the periodicity of the trace.

The whole rescaling procedure is now presented considering the homodyne trace with F_1 $OD = 8$ (Figure 5.6), but it has also been similarly applied to the other traces.

- We divide all the experimental data N_i (Figure 5.6) by the factor γ' (Figure 6.2 a).
- We perform a fit of the rescaled data with the function :

$$f(p) = f_0 + A \cos(\omega \cdot p + \phi_0), \quad (6.7)$$

taking f_0 , A , ω and ϕ_0 as free parameters.

- Using the parameters values obtained from the fit, we plot the rescaled data, subtracted by the offset f_0 , versus the values $\theta_i = \omega \cdot p_i + \phi_0$, calculated starting from the measured piezo positions p_i (Figure 6.2 b). The obtained fit curve is also shown in the plot .
- Being Δ the distance between two consecutive θ values for which the fit function goes to zero, we define the variable Φ such that $\Phi = \frac{\pi}{\Delta} \cdot \theta$.
- Finally we plot the rescaled data versus the values $\Phi_i = \frac{\pi}{\Delta} \cdot \theta_i$ and we report all the data in the interval $\Phi \in [0, 2\pi]$ (Figure 6.2 c). The fit obtained fit curve is also shown.

In the last trace (Figure 6.2 c) each point is given by a pair of measurements $(x_\Phi; \Phi)$, with $\Phi \in [0, 2\pi]$. As discussed in Section 1.2.2, from this experimental data set it is possible to completely characterize the *signal* field investigated with the homodyne detection.

6.2 Estimation of $\langle \hat{n} \rangle$

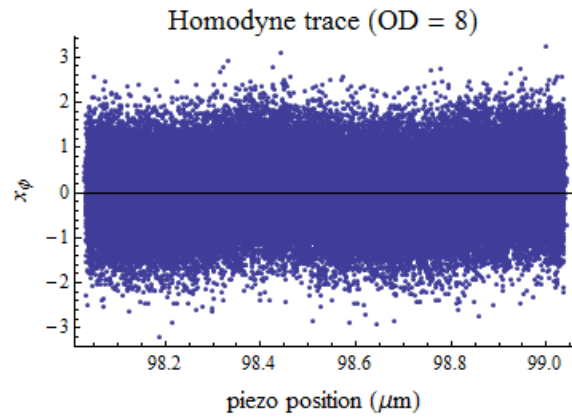
The first information one can obtain from the elaborated homodyne data (Figure 6.2 c) is the mean number of photons in the coherent *signal* field under investigation.

We know that the expectation value of the number operator \hat{n} on a coherent state $|\alpha\rangle$ is:

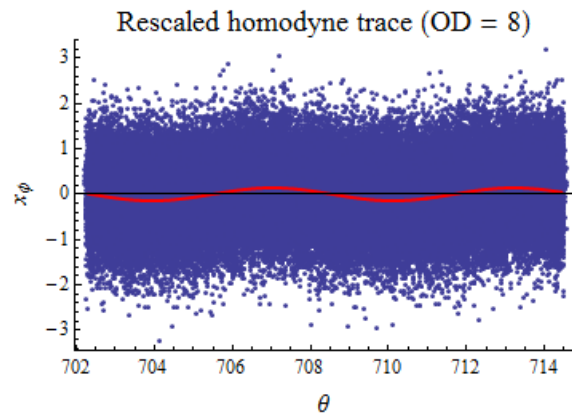
$$\langle \hat{n} \rangle = \langle \alpha | \hat{n} | \alpha \rangle = \langle \alpha | \hat{a}^\dagger \hat{a} | \alpha \rangle = |\alpha|^2 \quad (6.8)$$

and corresponds to the mean number of photons per pulse in the coherent state.

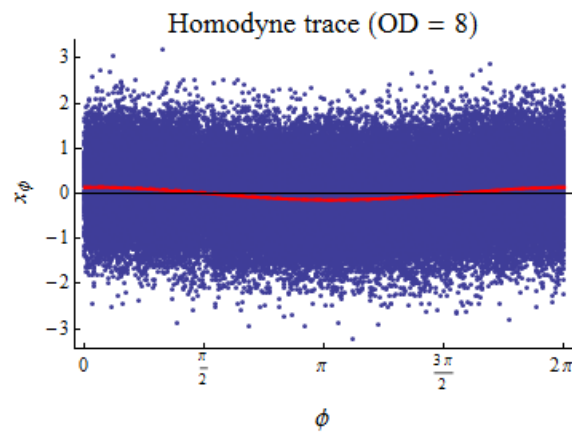
We can estimate $\langle \hat{n} \rangle = |\alpha|^2$ from the parameter A , obtained from the fit of



(a)



(b)



(c)

Figure 6.2: Data analysis procedure, homodyne trace with F_1 OD = 8.

our rescaled data with the function in (6.7). Comparing the equations (6.5) and (6.7), our estimation of the mean number of photons is the following:

$$\langle \hat{n} \rangle_{\gamma'} = \frac{|A|^2}{2}. \quad (6.9)$$

The results for all the homodyne traces are shown in Table (6.1), since the programming language *Mathematica* does not provide an error for the estimation of the fit parameter A , we consider as error in the estimation of $\langle \hat{n} \rangle_{\gamma'}$ the square root of the value. The obtained values are compared with n_{est} , calculated in the equation (5.1) starting from the power of the *signal* transmitted from the filter F_1 . The estimated $\langle \hat{n} \rangle_{\gamma'}$ for different traces results

F_1 OD	n_{est}	$\langle \hat{n} \rangle_{\gamma'}$
4.5	$1.9 \cdot 10^3$	14.6827
6	30	0.281914
7	3	0.042178
8	0.3	0.00996636

Table 6.1:

always about two orders of magnitude lower than n_{est} calculated using the equation (5.1).

We can attribute this discrepancy to the performance characteristics of the homodyne detector. The estimated $\langle \hat{n} \rangle_{\gamma'}$ is a sort of "effective" mean photon number, which includes all the losses and the inefficiencies of the detection system [33]. A very important source of inefficiency in our experimental apparatus is the electronic noise.

In the next section we will show in detail how we can take into account the effects of the electronic noise in our detector.

6.2.1 Electronic noise treatment

As explained in Section 4.2.3, any non-desiderable ambient noise, dark current noise from the photodiodes and the intrinsic noise of the amplifier in the differential photodetector are source of electronic noise (EN). The effect of such noise is to add a random quantity to each field quadrature measurement.

In reference [31], Appel et al. demonstrate that this effect is equivalent to an optical loss channel with equivalent transmission efficiency:

$$\eta_{eq} = 1 - \frac{1}{S}, \quad (6.10)$$

where S is the ratio between shot and electronic noises at the chosen LO power. In particular, the vacuum state measurement (Section 6.1.1) is distorted by the EN and consequently the rescaling factor γ' should be changed.

γ' is the conversion factor between the measured difference pulses and the field quadratures (equation 6.1) in presence of the electronic noise.

Following the treatment in the Appel's paper and considering the equation (6.4), we obtain the expression:

$$\gamma' = \sqrt{2 \langle N_{i0}^2 \rangle} = \frac{\gamma}{\sqrt{\eta_{eq}}}, \quad (6.11)$$

where γ is the conversion factor in case of absence of electronic noise.

After these considerations, we decided to repeat the data analysis using the conversion factor γ instead of γ' , in order to estimate the mean number of photons in the coherent *signal* field without considering the optical loss due to the EN presence.

6.2.2 New rescaling procedure

In Section 4.2.3 we analysed the linearity of the shot noise variance of our detector and we decided to work at $0.6 \text{ mW } LO$ power.

At this power, the shot-to-electronic noise ratio is $S = 1.2$ (Figure 4.7). This means that the EN constitutes a significant contribution to the measured noise.

From the equation (6.10) we calculate the value of η_{eq} for our homodyne detector and then we repeat the whole data analysis using the conversion factor

$$\gamma = \gamma' \cdot \sqrt{\eta_{eq}}. \quad (6.12)$$

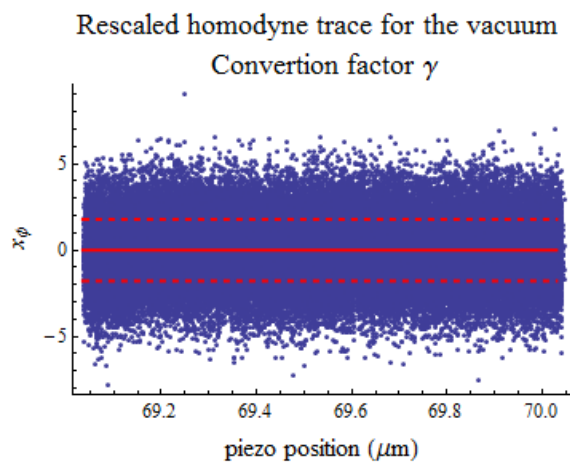


Figure 6.3: New rescaled homodyne trace of the vacuum state (γ conversion factor).

The new rescaled vacuum homodyne trace, for the homodyne trace with $OD = 8$, is shown in Figure (6.3).

The dotted red lines mark out the root mean square deviation of the new rescaled data : $\sqrt{\langle N_{i0}^2/\gamma \rangle} = 3.125$. As expected, this values is larger then $1/\sqrt{2} = \sigma[\hat{x}_\Phi]_{|0\rangle}$ (equation 6.3). This effect is due to the EN contribution to the homodyne trace.

The new rescaled homodyne trace with $OD = 8$ is reported in Figure 6.4.

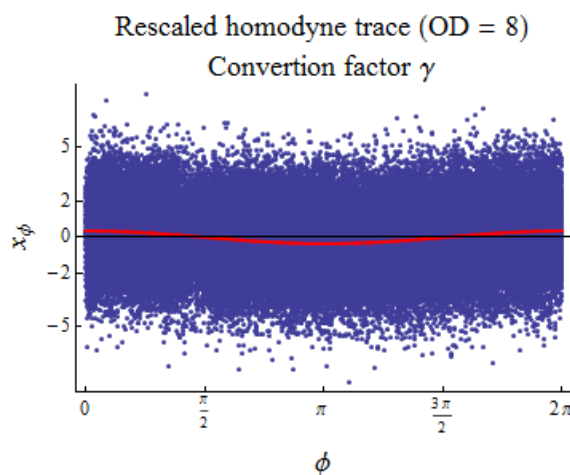


Figure 6.4: New rescaled *signal* ($OD = 8$) homodyne trace (γ conversion factor).

This new procedure allows us to estimate the mean number of photons in the *signal* coherent state, corrected from the *EN* effect:

$$\langle \hat{n} \rangle_\gamma = \frac{|A'|^2}{2} \cdot \frac{1}{\eta_{eq}} \quad (6.13)$$

where A' is the new amplitude parameter of the fit.

The analysis is repeated also for the homodyne traces in the other configurations of the filter F_1 , the results are shown in following table. It is immediate

F_1 OD	n_{est}	$\langle \hat{n} \rangle_\gamma$
4.5	$1.9 \cdot 10^3$	573.542
6	30	11.015
7	3	1.6488
8	0.3	0.389096

Table 6.2:

to observe that, with this procedure, the mean number of photons obtained by homodyne detection and calculated using the equation (5.1) now have the same order of magnitude for all the configurations.

It is also interesting to note that the approach in the reference [31], in treating the *EN* as an optical loss, is aimed at describing homodyne detectors with very high shot-to-electronic noise ratio. We have just shown that such kind of approach works also for a homodyne detector with low shot-to-electronic noise ratio.

6.3 Pattern function tomography

The homodyne measurement of the field quadratures $(x_\Phi; \phi)$, with $\phi \in [0, 2\pi]$, provides the complete knowledge of the state under investigation; indeed, the expectation value of any quantity of interest can be calculated, using the so called *pattern function tomography* technique [6].

6.3.1 Basic concepts

Given an arbitrary quantum system, the mean value $\langle \hat{O} \rangle$ of a generic system operator, can be estimated using only the results of the measurements on a

set of observables $\{\hat{Q}_\lambda, \lambda \in \Lambda\}$ called *quorum* (Section 1.1). This is possible through the estimator $R[\hat{O}](q; \lambda)$, called pattern function, which is a function of the eigenvalues q of the quorum operators. Integrating the estimator with the probability $p(q, \lambda)$ of having outcome q when measuring \hat{Q}_λ , the mean value of \hat{O} is obtained as follows:

$$\langle \hat{O} \rangle = \int_{\Lambda} d\lambda \int dq_\lambda p(q, \lambda) R[\hat{O}](q; \lambda), \quad (6.14)$$

where the first integral is performed on the values of λ that denote all quorum observables, and the second on the eigenvalues of the quorum observable q_λ determined by the λ variable of the outer integral.

In Optical Homodyne Tomography, the *quorum* of observables is composed by the quadrature operators: $\{\hat{x}_\Phi, \Phi \in [0, 2\pi]\}$. In this case the equation (6.14) becomes:

$$\langle \hat{O} \rangle = \int_0^{2\pi} \frac{d\Phi}{\pi} \int_{\mathbb{R}} dx p(x, \Phi) R[\hat{O}](x; \Phi), \quad (6.15)$$

where $p(x, \Phi)$ is the the probability distribution of the quadrature outcome at a fixed phase (equation 1.24).

In a homodyne measurement we obtain the following pair of experimental homodyne data: $\{(x_1; \Phi_1), (x_2; \Phi_2), \dots, (x_k; \Phi_k), \dots, (x_M; \Phi_M)\}$. Assuming know the pattern function of \hat{O} , the finite sum:

$$S_M = \frac{1}{M} \sum_{k=1}^M R[\hat{O}](x_k; \Phi_k) \quad (6.16)$$

gives an approximation of $\langle \hat{O} \rangle$ (equation 6.15). The error ϵ_M in such approximation can be estimated using the central limit theorem:

$$\epsilon_M = \sqrt{\frac{\sum_{k=1}^M [R[\hat{O}](x_k; \Phi_k) - S_M]^2}{M(M-1)}}. \quad (6.17)$$

6.3.2 Applications

The pattern function of the normally ordered products of mode operators is expressed as:

$$R[\hat{a}^{\dagger n} \hat{a}^m](x; \Phi) = e^{(m-n)\Phi} \frac{H_{n+m}(\sqrt{\eta}x_\Phi)}{\sqrt{(2\eta)^{n+m} \binom{n+m}{n}}}, \quad (6.18)$$

where H_k are the Hermite polynomial of order k . A complete treatment about the theoretical derivation of the pattern function expression is reported in [6].

The factor η in the definition (6.18) is the quantum efficiency of the homodyne detection apparatus. Our homodyne detector has an equivalent quantum efficiency $\eta_{eq} \approx 0.16$, due to a high electronic noise contribution. This corresponds to a shot-to-noise electronic ratio $S = 1.2$. This value is not sufficiently high to perform a complete quantum state reconstruction, since the EN blurs too much the quadrature distribution $p(x, \Phi)$ (equation 1.24). Nevertheless, we show in the following that by means of pattern function tomography we can evaluate of the mean number of photons in the coherent *signal* field under investigation.

From the equation (6.18) with ($n = m = 1$) we obtain:

$$R[\hat{a}^\dagger \hat{a}](x_\Phi; \Phi) = (x_\Phi)^2 - \frac{1}{2\eta}. \quad (6.19)$$

In order to correct for the EN loss effect, we put $\eta = \eta_{eq}$. Finally we estimate the mean photon number as:

$$\langle \hat{n} \rangle_{pattern} = \frac{1}{M} \sum_{k=1}^M R[\hat{a}^\dagger \hat{a}](x_k; \Phi_k) \frac{1}{\eta_{eq}}. \quad (6.20)$$

The error on this estimation is calculated using the equation (6.17). The results for the different homodyne traces are reported in Table 6.3 and compared with those obtained with the previous method, that is starting from the fit of the homodyne data. The estimations with the two methods are consistent.

F_1 OD	$\langle \hat{n} \rangle_\gamma$	$\langle \hat{n} \rangle_{pattern}$
4.5	573.542	557 ± 2
6	11.015	11.0 ± 0.2
7	1.6488	1.6 ± 0.1
8	0.389096	0.6 ± 0.1

Table 6.3:

In both cases we corrected the loss effect of the electronic noise substituting the nominal quantum efficiency of our differential detector $\eta = 0.77$ with the

equivalent quantum efficiency η_{eq} , calculated by the shot-to-electronic noise ratio $S = 1.2$ (equation 6.10) following [31].

The equation (6.18) can be used to obtain the pattern functions of the quadrature operator \hat{x}_Φ and of its square \hat{x}_Φ^2 at the specific phase $\Phi = \varphi$. Considering the quadrature operator definition (equation 1.21), its pattern function can be written as:

$$R[\hat{x}_\varphi](x, \Phi) = \frac{R[\hat{a}^{\dagger 0} \hat{a}^1](x; \Phi)e^{-i\varphi} + R[\hat{a}^{\dagger 1} \hat{a}^0](x; \Phi)e^{-i\varphi}}{\sqrt{2}} \quad (6.21)$$

$$= 2x \cos(\varphi - \Phi) \quad (6.22)$$

At this point we can evaluate the mean value of \hat{x}_φ using the pattern function tomography:

$$\langle \hat{x}_\varphi \rangle_{pattern} = \frac{1}{M} \sum_{k=1}^M R[\hat{x}_\varphi](x_k; \Phi_k) \quad \varphi \in [0, 2\pi]. \quad (6.23)$$

The result, for the filter configuration $OD = 8$, are shown in Figure 6.5 (red curve); the blue curve is the fit curve obtained with the previous method. The result shown in Figure 6.5 confirms the agreement between the pattern

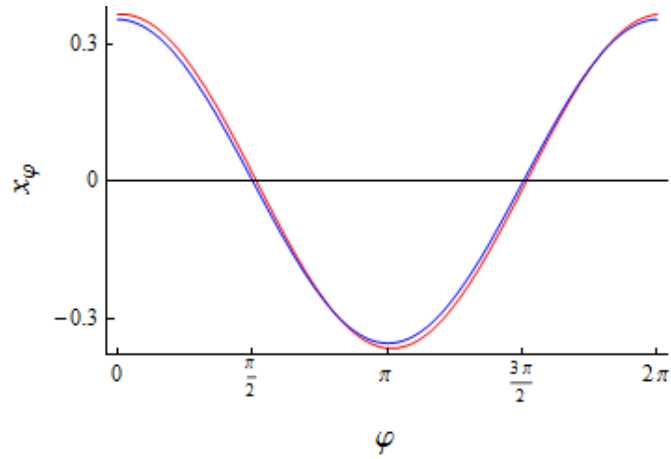


Figure 6.5: Red curve: estimation of the mean value of the quadrature using the pattern function tomography. Blue curve: fit of the experimental data obtained in Section (6.2.2). ($F_1 OD = 8$).

function tomography and the fit of the experimental data.

With the same approach used in the equation (6.21), we obtain the pattern function also of the operator \hat{x}_φ^2 :

$$R[\hat{x}_\varphi^2](x, \Phi) = \frac{1}{2} \left\{ 1 + \left(2x^2 - \frac{1}{\eta} \right) [4 \cos^2(\varphi - \Phi) - 1] \right\} \quad (6.24)$$

As before, we put $\eta = \eta_{eq}$ and we evaluate the mean value of \hat{x}_φ^2 :

$$\langle \hat{x}_\varphi^2 \rangle_{pattern} = \frac{1}{M} \sum_{k=1}^M R[\hat{x}_\varphi^2](x_k; \Phi_k) \quad \varphi \in [0, 2\pi]. \quad (6.25)$$

The result is used to estimate the quadrature variance as follows:

$$\sigma^2[\hat{x}_\varphi]_{pattern} = \langle \hat{x}_\varphi^2 \rangle_{pattern} - (\langle \hat{x}_\varphi \rangle_{pattern})^2 \quad \varphi \in [0, 2\pi]. \quad (6.26)$$

The obtained variance values are shown in Figure 6.6, for the filter configuration $OD = 8$.

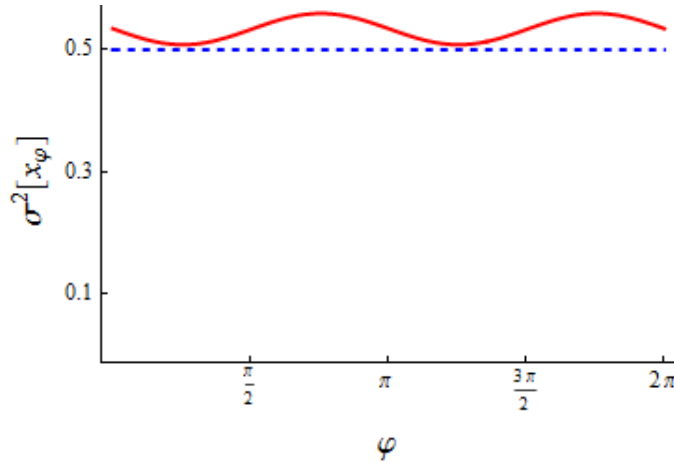


Figure 6.6: Estimation of the quadrature variance using the pattern function tomography (solid curve). Equivalent quantum efficiency η_{eq} (F_1 $OD = 8$).

The systematic periodicity of the calculated variance is an effect of the piezo position instability, treated in Section 5.3. The obtained curve oscillate around the value $\frac{1}{2}$, which is the expected quadrature variance for a coherent state (equation 6.6).

If we consider the nominal detector quantum efficiency $\eta = 0,77$ instead of η_{eq} in the equation (6.24), then we obtain the variance values shown in Figure

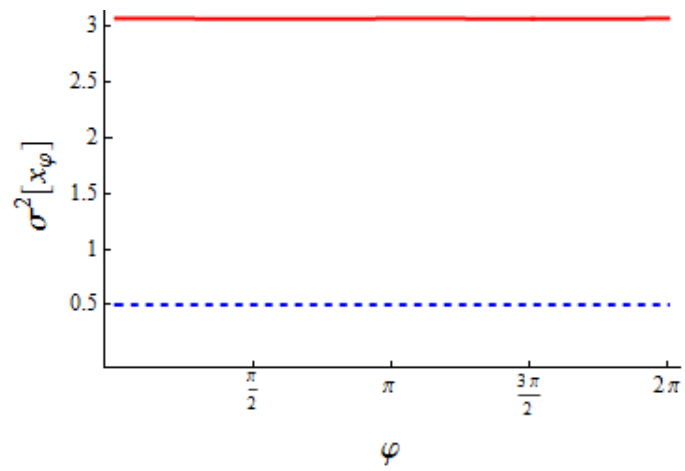


Figure 6.7: Estimation of the quadrature variance using the pattern function tomography (solid curve). Nominal quantum efficiency η ($F_1 OD = 8$).

6.7. As expected, the variance results higher than $\frac{1}{2}$, since the electronic noise adds a random quantity to each field quadrature measurement.

Appendix A

Density operator formalism

A physical system in Quantum Mechanics is associated to a Hilbert-space \mathcal{H} . In Section 1.1.1 we showed that the state of a generic quantum system is described by a density matrix $\hat{\rho}$ acting on \mathcal{H} . The density operator formalism is necessary in order to describe statistical ensembles of quantum systems, which can't be associated to a single vector in \mathcal{H} .

In order to clarify this concept, we consider an ensemble of particles such that each of the particles can be in either state $|a\rangle$ or $|b\rangle$ (but only one of them). We assume for instance that the classical probability of finding a particle in the state $|a\rangle$ or $|b\rangle$ is 50%.

It is evident that this system can't be described by the state vector $|\Psi\rangle = \frac{|a\rangle+|b\rangle}{\sqrt{2}}$, which represents a system in a state given by the linear superposition of $|a\rangle$ and $|b\rangle$ both with probability $\frac{1}{2}$.

The system in the example is instead in a mixed state, which is correctly described by the density operator

$$\hat{\rho} = \frac{1}{2} |a\rangle \langle a| + \frac{1}{2} |b\rangle \langle b|. \quad (\text{A.1})$$

If the particles in the ensemble are all prepared in the same state $|a\rangle$, then the system will be in a pure state described by the projector $|a\rangle \langle a|$.

We see immediately that the density operator formalism allows the description of both pure and mixed states. We can easily distinguish between a pure state and a mixed state using the density operator itself. For a pure

state,

$$\hat{\rho}^2 = \hat{\rho} \tag{A.2}$$

and the trace of the squared density operator is 1,

$$\text{Tr}[\hat{\rho}^2] = \text{Tr}[\hat{\rho}] = 1. \tag{A.3}$$

For a mixed state

$$\hat{\rho}^2 \neq \hat{\rho}, \tag{A.4}$$

and

$$\text{Tr}[\hat{\rho}^2] < 1. \tag{A.5}$$

In this sense $\text{Tr}[\hat{\rho}^2]$ is a measure of the purity of the system. When $\text{Tr}[\hat{\rho}^2] = 1$, the state is pure and can be described by a state-vector.

The complete information of a state is contained in the density operator. If we can somehow reconstruct the density operator in a representation, we know everything about the quantum state. For example, in Fock representation, the density matrix elements are $\rho_{nm} \equiv \langle n | \hat{\rho} | m \rangle$ [34].

Appendix B

Coherent states

A single mode of the radiation field is described by the mode operators \hat{a} and \hat{a}^\dagger , satisfying the bosonic commutation relation $[\hat{a}, \hat{a}^\dagger] = 1$.

A coherent state $|\alpha\rangle$ is defined as an eigenstate of the annihilation operator \hat{a} with an eigenvalue $\alpha \in \mathbb{C}$, i.e.,:

$$\hat{a} |\alpha\rangle = \alpha |\alpha\rangle. \quad (\text{B.1})$$

It is possible to write a coherent state in terms of photon number eigenstates $|n\rangle$:

$$|\alpha\rangle = \sum_{n=0}^{\infty} c_n |n\rangle. \quad (\text{B.2})$$

The coefficients c_n are given from the equations (B.1) and (B.2) as follows:

$$\hat{a} |\alpha\rangle = \sum_{n=0}^{\infty} c_n \hat{a} |n\rangle = \sum_{n=1}^{\infty} c_n \sqrt{n} |n-1\rangle = \sum_{n=0}^{\infty} c_{n+1} \sqrt{n+1} |n\rangle = \alpha |\alpha\rangle; \quad (\text{B.3})$$

from the last equality in (B.3) we obtain

$$c_{n+1} = \frac{\alpha c_n}{\sqrt{n+1}} \quad (\text{B.4})$$

and by recursion

$$c_n = c_0 \frac{\alpha^n}{\sqrt{n!}}. \quad (\text{B.5})$$

The coefficient c_0 is obtained from the normalization condition $\langle\alpha|\alpha\rangle = 1$, which, by using (B.2), gives $c_0 = e^{-|\alpha|^2/2}$.

The final result is:

$$|\alpha\rangle = e^{-\frac{|\alpha|^2}{2}} \sum_{n=0}^{\infty} \frac{\alpha^n}{\sqrt{n!}} |n\rangle, \quad (\text{B.6})$$

which we showed in section (1.2.1) without proof.

We now prove also the expression (1.16) in which the coherent state is written as the displacement operator acting on the vacuum state.

Since $|n\rangle = [(\hat{a}^\dagger)^n / \sqrt{n!}] |0\rangle$ the equation (B.6) becomes

$$|\alpha\rangle = e^{-\frac{|\alpha|^2}{2}} e^{\alpha \hat{a}^\dagger} |0\rangle; \quad (\text{B.7})$$

by considering the fact that $e^{(-\alpha^* \hat{a})} |0\rangle = |0\rangle$, the equation (B.7) can be rewritten as:

$$|\alpha\rangle = D(\alpha) |0\rangle, \quad (\text{B.8})$$

where

$$D(\alpha) = e^{-\frac{|\alpha|^2}{2}} e^{-\alpha^* \hat{a}} e^{\alpha \hat{a}^\dagger} \quad (\text{B.9})$$

is a unitary operator, it will be demonstrated it is equivalent to the displacement operator defined in the equation (1.17).

By using the *Baker-Hausdorff* formula: given A and B any two operators such that

$$[[A, B], A] = [[A, B], B] = 0, \quad (\text{B.10})$$

then

$$e^{A+B} = e^{(-[A,B]/2)} e^A e^B. \quad (\text{B.11})$$

If we impose $\hat{A} = \alpha \hat{a}^\dagger$ and $\hat{B} = -\alpha^* \hat{a}$, it follows that the operator in (B.9) becomes

$$D(\alpha) = e^{(\alpha \hat{a}^\dagger - \alpha^* \hat{a})}, \quad (\text{B.12})$$

which is the standard definition of the displacement operator as introduced in (1.17).

$D(\alpha)$ is a unitary operator, $D^\dagger(\alpha) = D(-\alpha) = D^{-1}(\alpha)$, which act as a displacement on the creation and annihilation operators:

$$D^\dagger(\alpha) \hat{a} D(\alpha) = \hat{a} + \alpha, \quad (\text{B.13})$$

$$D^\dagger(\alpha) \hat{a}^\dagger D(\alpha) = \hat{a}^\dagger + \alpha^*. \quad (\text{B.14})$$

The displacement property (B.13) is now proved by writing

$$D^\dagger(\alpha)\hat{a}D(\alpha) = e^{(\alpha^*\hat{a}-\alpha\hat{a}^\dagger)}\hat{a}e^{(\alpha\hat{a}^\dagger-\alpha^*\hat{a})}, \quad (\text{B.15})$$

and considering the following identity valid for arbitrary operators A and B :

$$\begin{aligned} e^A B e^{-A} &= \sum_{k=0}^{\infty} \frac{1}{k!} \underbrace{[A, [A, \dots [A, B \dots]]}_{k \text{ times}} \\ &= A + \frac{[A, B]}{1!} + \frac{[A, [A, B]]}{2!} + \dots; \end{aligned} \quad (\text{B.16})$$

for $A = (\alpha^*\hat{a} - \alpha\hat{a}^\dagger)$, $B = \hat{a}$ and since $[\hat{a}, \hat{a}^\dagger] = 1$, we can easily obtain the property in (B.13). The displacement property in (B.14) can be proved in a similar way.

Another important property of the coherent states is that the probability $p(m)$ of finding m photons in $|\alpha\rangle$ is given by a Poisson distribution. Indeed, from the equation (B.6) the following result is immediate to verify:

$$p(m) = |\langle m|\alpha\rangle|^2 = \left| e^{-\frac{|\alpha|^2}{2}} \sum_{n=0}^{\infty} \frac{\alpha^n}{\sqrt{n!}} \langle m|n\rangle \right|^2 = \frac{e^{-|\alpha|^2} |\alpha|^{2m}}{m!} = \frac{e^{-\langle n\rangle} \langle n\rangle^m}{m!}. \quad (\text{B.17})$$

In the last equality we use that the expectation value of the number operator on a coherent state is $\langle n\rangle = \langle \alpha|\hat{a}^\dagger\hat{a}|\alpha\rangle = |\alpha|^2$.

Appendix C

Homodyne detection formalism in pulsed regime

Balanced Homodyne Detection in pulsed regime requires a formal generalization of its theoretical description (Chapter 2), since the local oscillator and the signal at the beam splitter are not monochromatic. This issue has been poorly treated in the literature on the subject. In this appendix we developed a mathematical formalism that generalizes the theoretical treatment of the single-mode Balanced Homodyne Detection to the pulsed regime.

As we showed in Section 3.1.1, classically the electric field of a pulsed laser beam is a mode-locked superposition of amplitudes:

$$E(t) = \sum_{l=-M}^M |\alpha_l| e^{i \overbrace{(\omega_l t + \varphi_l)}^{\Phi_l(t)}}, \quad (\text{C.1})$$

where the phases $\Phi_l(t) = \omega_l t + \varphi_l$ contain the mode-locking condition $\varphi_l = l \varphi_0$.

In (3.1) we considered for simplicity the same amplitude for each contributing frequency ω_l ; here we generalize that expression by setting $\alpha_l = |\alpha_l| e^{i\Phi_l}$ and. The number $2M + 1$ of contributing frequencies depends on the shape of the pulse.

As showed in reference [35], pulsed laser light can be treated in a quantized framework by associating to each monochromatic component a coherent

state and to the field $E(t)$ the tensor product of the coherent states of each contributing frequency.

As showed in Appendix B, a monochromatic coherent state for the l mode is:

$$|\alpha_l\rangle = D(\alpha_l) |0\rangle, \quad (\text{C.2})$$

where $D(\alpha_l)$ is the displacement operator defined in (B.12) and $|0\rangle$ is the vacuum state. In this case:

$$D(\alpha_l) = e^{(\alpha_l \hat{a}_l^\dagger - \alpha_l^* \hat{a}_l)}, \quad (\text{C.3})$$

with \hat{a}_l and \hat{a}_l^\dagger the annihilation and creation operators of a photons of frequency ω_l . The commutation relations in this case are

$$[\hat{a}_i, \hat{a}_j^\dagger] = \delta_{ij}; \quad (\text{C.4})$$

finally, the displacement property in (B.13) can be generalized as:

$$D^\dagger(\alpha_j) \hat{a}_l D(\alpha_j) = D(-\alpha_j) \hat{a}_l D(\alpha_j) = \hat{a}_l + \alpha_l \delta_{jl}, \quad (\text{C.5})$$

We can now write the coherent state associated to the laser pulse as:

$$|\bar{\alpha}\rangle = \bigotimes_{l=-M}^M |\alpha_l\rangle = \exp\left(\sum_{l=-M}^M (\alpha_l \hat{a}_l^\dagger - \alpha_l^* \hat{a}_l)\right) |0\rangle, \quad (\text{C.6})$$

where $\bar{\alpha}$ is a vector, whose components are the amplitudes α_l . We have regrouped all exponentials into one using $[\hat{a}_i, \hat{a}_j^\dagger] = 0$ for different frequencies ($i \neq j$).

The reason for labeling the state by $|\bar{\alpha}\rangle$ can be easily understood. The state of one photon of frequency ω_l is given by $\hat{a}_l^\dagger |0\rangle = |1_l\rangle$. If one photon is in a non-monochromatic superposition of frequencies ω_l with amplitudes α_l , we write the state as $|1_{\bar{\alpha}}\rangle = \sum_l \alpha_l |1_l\rangle$; it can be expressed as the result of the action on the vacuum of a new creation operator

$$\hat{A}^\dagger(\bar{\alpha}) = \sum_l \alpha_l \hat{a}_l^\dagger, \quad (\text{C.7})$$

such that

$$\hat{A}^\dagger(\bar{\alpha}) |0\rangle = \sum_l \alpha_l \hat{a}_l^\dagger |0\rangle = \sum_l \alpha_l |1_l\rangle = |1_{\bar{\alpha}}\rangle. \quad (\text{C.8})$$

In this formalism $\langle \bar{\alpha} \rangle$ turns out to be the coherent state with amplitudes α_l . Indeed, given

$$\hat{A}(\bar{\alpha}) = \sum_l \alpha_l^* \hat{a}_l \quad (\text{C.9})$$

and using (C.4), one can compute the following generalized commutation relations:

$$\left[\hat{A}(\bar{\alpha}), \hat{A}^\dagger(\bar{f}) \right] = \sum_{ij} \alpha_i^* f_j [\hat{a}_i, \hat{a}_j^\dagger] = \sum_i \alpha_i^* f_i = \langle 1_{\bar{\alpha}} | 1_{\bar{f}} \rangle. \quad (\text{C.10})$$

From the substitution of the definitions (C.7) and (C.9) into (C.6), we finally obtain:

$$|\bar{\alpha}\rangle = e^{\hat{A}^\dagger(\bar{\alpha}) - \hat{A}(\bar{\alpha})} |0\rangle. \quad (\text{C.11})$$

Thus, the quantum state of the pulsed laser is a coherent state associated not to a single amplitude α_l , but to the vector $\bar{\alpha}$ of all the amplitudes contributing to the pulse: in other words, we have a Poissonian distribution not with respect to the number of photons in a monochromatic wave, but to the number of photons in the superposition $|\bar{\alpha}\rangle$.

A last technically useful relation is a generalization of the displacement property in (C.5). Being

$$D(\bar{f}) = e^{\hat{A}^\dagger(\bar{f}) - \hat{A}(\bar{f})}, \quad |\bar{f}\rangle = D(\bar{f}) |0\rangle \quad \text{and} \quad |1_{\bar{f}}\rangle = \sum_l f_l |1_l\rangle, \quad (\text{C.12})$$

using the identity in (B.16) and the generalized commutation relations in (C.10), we can obtain:

$$D^\dagger(\bar{f}) \hat{A}(\bar{\alpha}) D(\bar{f}) = D(-\bar{f}) \hat{A}(\bar{\alpha}) D(\bar{f}) = \hat{A}(\bar{\alpha}) + \langle 1_{\bar{\alpha}} | 1_{\bar{f}} \rangle. \quad (\text{C.13})$$

By means of this new formalism we can describe the state of a pulsed laser and we can generalize the expectation value of the homodyne photocurrent (equation 2.9) to the case in which the *signal* and the *Local Oscillator* are pulsed.

If more frequencies ω_l are present both in the *Local Oscillator* and in the *Signal*, each one of the corresponding mode operators will be subjected to the beam splitting transformation (2.4) and the detectors will ideally register photons of all involved frequencies.

Therefore, the generalization of the difference photocurrent operator, given in (2.5), will be:

$$\hat{I} = \sum_l \hat{c}_l^\dagger \hat{c}_l - \hat{d}_l^\dagger \hat{d}_l = \sum_l \hat{a}_l^\dagger \hat{b}_l + \hat{b}_l^\dagger \hat{a}_l \quad (\text{C.14})$$

We now consider the *Local Oscillator* incoming state given by $|\bar{z}\rangle\langle\bar{z}|$, such that $|\bar{z}\rangle = e^{\hat{B}^\dagger(\bar{z}) - \hat{B}(\bar{z})} |0\rangle$, where the generalized creation and annihilation operators are:

$$\hat{B}^\dagger(\bar{z}) = \sum_l z_l \hat{b}_l^\dagger, \quad \hat{B}(\bar{z}) = \sum_l z_l^* \hat{b}_l. \quad (\text{C.15})$$

As explained in Section 2.1, there is a fixed phase difference Φ between the *LO* and the *signal* state $\hat{\rho}_s$; it is due to the action of a piezoelectric translator placed in the *LO* arm in the Balanced Homodyne Detector. This means that all the *LO* modes are subjected to a phase shift:

$$\begin{aligned} \hat{b}_l &\rightarrow \hat{b}_l e^{i\Phi} \\ \hat{b}_l^\dagger &\rightarrow \hat{b}_l^\dagger e^{-i\Phi}. \end{aligned} \quad (\text{C.16})$$

The homodyne current will be evaluated as:

$$\begin{aligned} \langle \hat{I}_\Phi \rangle &= \sum_l \left(\text{Tr} \left[\hat{\rho}_s \otimes |\bar{z}\rangle\langle\bar{z}| \left(\hat{a}_l^\dagger \hat{b}_l e^{i\Phi} + \hat{b}_l^\dagger \hat{a}_l e^{-i\Phi} \right) \right] \right) \\ &= \sum_l \left(\text{Tr} \left[\hat{\rho}_s \otimes |\bar{z}\rangle\langle\bar{z}| \left(\hat{a}_l^\dagger \hat{b}_l e^{i\Phi} \right) \right] + h.c. \right) \\ &= \sum_l \left(\text{Tr} \left[\hat{\rho}_s \hat{a}_l^\dagger \right] \cdot \text{Tr} \left[|\bar{z}\rangle\langle\bar{z}| \hat{b}_l e^{i\Phi} \right] + h.c. \right) \\ &= \sum_l \left(\text{Tr} \left[\hat{\rho}_s \hat{a}_l^\dagger \right] \cdot \langle \bar{z} | \hat{b}_l | \bar{z} \rangle e^{i\Phi} + h.c. \right). \end{aligned} \quad (\text{C.17})$$

Using the identity in (B.16), we can show the following result:

$$\begin{aligned} \langle \bar{z} | \hat{b}_l | \bar{z} \rangle &= \langle 0 | e^{-\hat{B}^\dagger(\bar{z}) + \hat{B}(\bar{z})} \hat{b}_l e^{\hat{B}^\dagger(\bar{z}) - \hat{B}(\bar{z})} | 0 \rangle \\ &= \langle 0 | [-\hat{B}^\dagger(\bar{z}), \hat{b}_l] | 0 \rangle = z_l. \end{aligned} \quad (\text{C.18})$$

In a similar way we can prove that $\langle \bar{z} | \hat{b}_l^\dagger | \bar{z} \rangle = z_l^*$. Thus, the expectation value

in (C.17) becomes:

$$\begin{aligned}
\langle \hat{I}_\Phi \rangle &= \sum_l \left(\text{Tr} \left[\hat{\rho}_s \hat{a}_l^\dagger \right] \cdot z_l e^{i\Phi} + h.c. \right) \\
&= \sum_l \left(\text{Tr} \left[\hat{\rho}_s \hat{a}_l^\dagger \right] \cdot z_l e^{i\Phi} + \text{Tr} \left[\hat{\rho}_s \hat{a}_l \right] \cdot z_l^* e^{-i\Phi} \right) \\
&= \sum_l \left(\text{Tr} \left[\hat{\rho}_s \left(\hat{a}_l^\dagger z_l e^{i\Phi} + \hat{a}_l z_l^* e^{-i\Phi} \right) \right] \right) \\
&= \text{Tr} \left[\hat{\rho}_s \left(\hat{A}^\dagger(\bar{z}) e^{i\Phi} + \hat{A}(\bar{z}) e^{-i\Phi} \right) \right]. \tag{C.19}
\end{aligned}$$

In the last equality, we used the definitions in (C.7) and (C.9), which in this case are $\hat{A}(\bar{z}) = \sum_l z_l^* \hat{a}_l$ and $\hat{A}^\dagger(\bar{z}) = \sum_l z_l \hat{a}_l^\dagger$.

Furthermore, suppose the *signal* state $\hat{\rho}_s = |\bar{\alpha}\rangle\langle\bar{\alpha}|$ is another non-monochromatic coherent state, then the result in (C.19) becomes:

$$\langle \hat{I}_\Phi \rangle = \langle \bar{\alpha} | \hat{A}^\dagger(\bar{z}) | \bar{\alpha} \rangle e^{i\Phi} + \langle \bar{\alpha} | \hat{A}(\bar{z}) | \bar{\alpha} \rangle e^{-i\Phi} = \langle 1_{\bar{\alpha}} | 1_{\bar{z}} \rangle e^{i\Phi} + \langle 1_{\bar{z}} | 1_{\bar{\alpha}} \rangle e^{-i\Phi}; \tag{C.20}$$

where we used the result in (C.13) to demonstrate that:

$$\langle \bar{\alpha} | \hat{A}(\bar{z}) | \bar{\alpha} \rangle = \langle 0 | D(-\bar{\alpha}) \hat{A}(\bar{z}) D(\bar{\alpha}) | 0 \rangle = \langle 1_{\bar{z}} | 1_{\bar{\alpha}} \rangle, \tag{C.21}$$

and similarly $\langle \bar{\alpha} | \hat{A}^\dagger(\bar{z}) | \bar{\alpha} \rangle = \langle 1_{\bar{\alpha}} | 1_{\bar{z}} \rangle$.

Since in a Balanced Homodyne Detection the *signal* and the *LO* come from the same pulsed laser source, we can consider $\bar{z} = \bar{\alpha}$, it follows that the equation in (C.20) becomes: $\langle \hat{I}_\Phi \rangle = 2 \langle 1_{\bar{z}} | 1_{\bar{z}} \rangle \cos \Phi$.

Comparing these results with the ones obtained in Chapter 2 for the single-mode case, one realizes that in the pulsed *BHD* correctly measures the quadrature $\hat{x}_\Phi = \hat{A}^\dagger(\bar{z}) e^{i\Phi} + \hat{A}(\bar{z}) e^{-i\Phi}$ associated with the pulsed field laser of amplitude $|\bar{z}| = \sqrt{\langle 1_{\bar{z}} | 1_{\bar{z}} \rangle}$.

For this reason, in the main text of the thesis we have limited the discussion to the simpler case of a single mode *BHD*, with the proviso that whenever quadrature \hat{x}_Φ and amplitude $|z|$ are used, they actually refer to the pulsed ones $\hat{x}_\Phi = \hat{A}^\dagger(\bar{z}) e^{i\Phi} + \hat{A}(\bar{z}) e^{-i\Phi}$ and $|z| = \sqrt{\langle 1_{\bar{z}} | 1_{\bar{z}} \rangle}$. In particular, when the input *signal* state is the vacuum $|0\rangle$, then $\langle I_\Phi \rangle = 0$, as in the single mode

case; further, for an attenuated input state $|\epsilon \bar{z}\rangle$ ($0 < \epsilon < 1$), one regains the results in Section 2.3: $\langle \hat{I}_\Phi \rangle = 2\epsilon |\bar{z}|^2 \cos \Phi$.

We have thus generalized the treatment of a monochromatic *BHD*, to the case of pulsed input light; it explicitly takes in account the fact that the state of a pulsed laser is the tensor product of the coherent states of each contributing frequency. This is of great importance for the future applications of the realized apparatus to time-resolved spectroscopy experiments.

Conclusions

Balanced Homodyne Detection (BHD) is one of the most powerful experimental technique in Quantum Optics; through the measurements of the electromagnetic field quadratures it allows the complete reconstruction of the optical quantum states (*Optical Homodyne Tomography*).

In this thesis we described the realization of an experimental apparatus for the *BHD* in a pulsed regime. In the first part, a theoretical treatment of the *BHD* is presented in detail; in particular, we generalized the standard theoretical treatment of the *BHD* in order to describe the pulsed regime. Afterwards, a description of the experimental apparatus and its performances is given.

As in standard *BHD* scheme, the field we want to study, called *signal*, interferes at a 50% *beam-splitter* with a strong coherent reference beam, called *Local Oscillator (LO)*. The outputs are collected by two photodiodes and the difference in the produced photocurrents is measured by a commercial differential photodetector. The measured photocurrents are proportional to the field quadratures expectation values x_{Φ} , where the phase Φ is varied by means of a piezo-electric translator. The *signal* and the *LO* are generated by a pulsed laser source with 80 MHz repetition rate.

We characterized the apparatus, both from the point of view of the mechanical stability and from that of the differential acquisition system. We checked that the temporal resolution of the detection system is sufficient to provide independent measurements of each pair of pulses impinging on the differential photodetector. We measured the shot-to-electronic noise ratio ($S = 1.2$), discovering that the electronic noise constitutes a significant contribution

to the our apparatus noise; the shot noise reflects the statistics of the light amplitude fluctuations for different phase values, while the effect of the electronic noise is to blur such statistics.

After the characterization measurements, we used the apparatus to perform homodyne measurements of pulsed coherent states with different mean number of photons. In particular, we managed to observe the variation with Φ of the mean field quadrature of coherent states with a mean number of photon of the order of unity or less.

We analyse the obtained homodyne data, also taking into account the effects due to the presence of the electronic noise. In particular, we verify that the electronic noise treatment in the reference [31] is valid also in our case, despite the fact that the shot-to-electronic noise ratio is much higher in our apparatus than in the one described there.

Finally we used the *pattern function tomography* technique to estimate the mean values a few observables of the investigated coherent states, such as the number operator and the quadrature operator itself. In particular, we verified that the expectation value of the number operator, calculated by the *pattern function tomography*, is consistent with an independent estimation obtained starting from the measurement of the *signal* beam power.

To the best of our knowledge, the realized experimental apparatus is the first *Balanced Homodyne Detector* built with a commercial differential photodetector. Despite the rather high shot-to-electronic noise ratio, it performs extremely well, allowing the analysis of *signal* inputs containing an average of less than one photon per pulse.

The realization of the apparatus is a very important and promising step forward in the ongoing project of applying pulsed *BHD* to time-resolved spectroscopy experiment.

Riassunto dettagliato

Questo lavoro di tesi consiste nello studio teorico e nella realizzazione sperimentale di un apparato per la *Rivelazione Omodina Bilanciata* in regime impulsato. Questa tecnica, indicata con il termine inglese *Balance Homodyne Detection (BHD)*, permette di caratterizzare, o meglio “misurare” stati quantistici della luce [11].

In Meccanica Quantistica, la luce, come ogni altro sistema fisico, è descritta infatti dal suo stato quantistico. Gli esempi più semplici di stati quantistici della radiazione elettromagnetica a singolo modo, ovvero caratterizzata da una determinata frequenza e polarizzazione, sono i così detti *stati di Fock*, che descrivono un sistema di n fotoni nel modo considerato; i tipici stati quantistici della luce generata da una sorgente laser ideale sono invece i così detti *stati coerenti*.

“Misurare” lo stato quantistico di un generico sistema fisico significa caratterizzarlo completamente, ovvero avere su di esso la massima informazione, che, in Meccanica Quantistica, si traduce nel poter calcolare il valore di aspettazione di qualsiasi sua osservabile fisica. È stato dimostrato [6] che da misure ripetute di un certo insieme di osservabili di un sistema fisico è possibile ricostruire lo stato quantistico del sistema stesso; lo specifico insieme di osservabili è detto *quorum*, la procedura di ricostruzione dello stato è detta *tomografia quantistica*.

Nel nostro caso, il sistema fisico in esame, di cui vogliamo determinare lo stato quantistico, è la luce generata da un laser impulsato, attenuata in modo da avere un bassissimo numero medio di fotoni per impulso, dell'ordine

dell'unità e inferiore; il *quorum* di osservabili è costituito dalle *quadrature* del campo elettromagnetico, tali osservabili sono combinazioni lineari degli operatori di posizione e momento associati all'oscillatore armonico che descrive il modo della radiazione. La *BHD* ci permette di misurare tali quadrature e da queste misure di ricostruire lo stato quantistico attraverso tecniche di tomografia quantistica, nello specifico *Optical Homodyne Tomography* [19].

Descriviamo ora brevemente la procedura di *misura omodina*. Il campo in esame, detto *segnale*, interferisce su di un beam-splitter con un secondo campo molto più intenso, detto *oscillatore locale*, i due campi provengono dalla stessa sorgente laser impulsata che genera, sfruttando la tecnica del mode-locking, un treno di impulsi della durata di circa 10^{-13} secondi. Variando il cammino ottico di uno dei due campi con un traslatore piezoelettrico è possibile variare la loro differenza di fase Φ . I fasci in uscita dal beam splitter vengono focalizzati su due fotodiodi e la differenza tra le foto-correnti generate viene amplificata e misurata. Dal modello teorico è possibile dimostrare che la misura di questa corrente differenza fornisce una stima della quadratura del campo in esame. Misure di quadratura per diversi valori della fase Φ costituiscono la così detta *misura omodina* da cui si può determinare lo stato quantistico del *segnale*. La novità del nostro apparato è che si sono utilizzati esclusivamente strumenti commerciali per la rivelazione della corrente differenza.

La tecnica omodina è ampiamente utilizzata per caratterizzare stati quantistici della radiazione sia in regime continuo che in regime impulsato [33]. Pochi gruppi al mondo ([22, 23, 24, 25]) però sono riusciti ad utilizzare questa tecnica per caratterizzare stati quantistici di luce impulsata con il tasso di ripetizione tipico dei laser a mode-locking: circa 80 MHz. Il regime impulsato infatti comporta non poche difficoltà sperimentali, poiché oltre alla stabilità opto-meccanica è necessario un sistema di rivelazione veloce e a basso rumore elettronico in grado di effettuare misure di quadratura indipendenti per ogni coppia di impulsi che interferiscono sul beam-splitter. In questa tesi si è scelto di lavorare in regime mode-locking impulsato, nella prospettiva futura di utilizzare il rivelatore omodino in esperimenti

di spettroscopia di materiali nel dominio dei tempi. Riuscire a misurare infatti lo stato quantistico della radiazione impulsata prima e dopo aver interagito con un campione di materiale, può in linea di principio fornire informazioni su stati di eccitazione che possono crearsi nel campione, come ad esempio stati vibrazionali coerenti. La realizzazione di un rivelatore omodino impulsato è il punto di partenza di questo nuovo obiettivo di ricerca, nato dalla collaborazione tra il gruppo teorico del dott. Fabio Benatti e del dott. Roberto Floreanini presso il Dipartimento di Fisica dell'Università di Trieste e il gruppo sperimentale *T-Rex* coordinato dal prof. Fulvio Parmigiani presso *Elettra-Sincrotrone Trieste*.

Anche il lavoro di tesi è diviso in una parte teorica ed in una sperimentale. La parte teorica è così sviluppata:

- si sono delineate le base teoriche di Ottica Quantistica necessarie a descrivere gli stati quantistici della luce in esame, introducendo il formalismo degli *stati di Fock* e degli *stati coerenti* e si è approfondito il concetto di tomografia quantistica per un generico sistema fisico, tale studio è riportato nel Capitolo 1 e nelle Appendici A e B;
- si è studiato il modello teorico standard che descrive la tecnica di rivelazione omodina di un singolo modo della radiazione elettromagnetica (Capitolo 2), calcolando quali sono le condizioni per cui la misura della corrente differenziale in un rivelatore omodino fornisce una stima della quadratura del campo in esame;
- si è sviluppato un formalismo matematico che permette di generalizzare il modello standard della rivelazione omodina a singolo modo al caso del regime impulsato: classicamente il campo elettrico di un impulso di luce è descritto dalla sovrapposizione di più modi longitudinali della cavità laser (Sezione 3.1.1), il problema di descrivere lo stato quantistico di un campo ottico impulsato è invece poco trattato in letteratura, il formalismo da noi sviluppato permette di descrivere tale tipo di stato quantistico ottico e quindi di generalizzare il modello della rivelazione omodina al caso in cui l'*oscillatore locale* e il *segnale* sono impulsati; tale trattazione è presentata in Appendice C.

La parte sperimentale della tesi riguarda invece l'effettiva realizzazione e caratterizzazione del rivelatore omodino e la verifica del suo funzionamento tramite la misura delle quadrature di campi *segnale* con un numero medio di fotoni per impulso $\langle n \rangle \simeq 1$ e inferiore. Bloccando il fascio *segnale* in ingresso nel beam-splitter abbiamo effettuato una misura omodina anche per lo stato di *vuoto di Fock*. Le fasi del lavoro sperimentale sono le seguenti:

- si è costruito l'apparato considerandolo diviso in tre parti: sorgente impulsata, set up opto-meccanico e sistema di rivelazione e acquisizione; si è usata la sorgente impulsata al Ti:Sapphire (*Mira seed*) presente nei laboratori *T-Rex* a *Elettra-Sincrotrone*, il set up opto-meccanico è stato assemblato da zero e connesso al sistema di rivelazione composto da un foto-rivelatore differenziale commerciale collegato ad un oscilloscopio digitale e ad un pc; alcuni softwares sono stati sviluppati con il linguaggio di programmazione *Lab-View* per gestire e interfacciare il sistema opto-meccanico e il sistema di rivelazione; la strumentazione completa è descritta nel Capitolo 3;
- si sono effettuate misure di caratterizzazione dell'apparato per quel che riguarda sia la stabilità opto-meccanica che il sistema di acquisizione differenziale in regime impulsato, esse sono presentate nel Capitolo 4; il principale risultato è che il sistema è in grado di misurare indipendentemente la corrente differenza dovuta a due coppie successive di impulsi interferenti, ma, nella misura di quadratura del vuoto (campo segnale bloccato), il rumore risulta per più della metà costituito da rumore elettronico e solo una piccola parte è rappresentata dal rumore intrinseco (shot-noise); l'effetto del rumore elettronico è di aggiungere una quantità random alle varie misure di quadratura, si è tenuto conto di quest'effetto nell'analisi dati;
- si è poi proceduto ad effettuare le misure omodina vere e proprie per campi *segnale* con diversi numeri di fotoni medi per impulso; ciascuna così detta *traccia omodina* è costituita da 80000 dati fatti da coppie *corrente differenza-posizione piezo*, che in tutti i casi mostrano la tipica periodicità attesa per uno stato coerente in uscita dal laser impulsato, le misure sono mostrate nel Capitolo 5;

-
- le tracce omodine sono state analizzate in modo da trasformare i dati in coppie *quadratura-fase*; a partire da questi dati sperimentali abbiamo calcolato il valore di aspettazione del numero medio di fotoni per ciascuna traccia tramite una particolare tecnica tomografica detta *pattern function tomography* [6]; tale valore è stato confrontarlo con una stima indipendente ottenuta a partire dalla misura della potenza del fascio *segnale*; tenendo conto degli effetti dovuti al rumore elettronico [31], le due stime risultano consistenti; l'analisi dati completa è presentata nel Capitolo 6.

Concludendo, l'obiettivo della tesi può dirsi raggiunto, in quanto l'apparato di *Balanced Homodyne Detection* è stato realizzato e caratterizzato in regime impulsato utilizzando esclusivamente strumenti commerciali per la rivelazione differenziale. Si è dimostrato che il rivelatore può misurare tracce omodina di campi *segnale* con numero medio di fotoni per impulso $\langle n \rangle \simeq 1$ e inferiore. La realizzazione e la caratterizzazione di questo apparato costituiscono un promettente primo passo per l'utilizzo del metodo di rivelazione omodina impulsata in esperimenti di spettroscopia dei materiali nel dominio dei tempi, obiettivo questo del progetto di ricerca teorico-sperimentale in cui si colloca la tesi stessa.

Bibliography

- [1] U. Fano. “Description of states in quantum mechanics by density matrix and operator techniques”. In: *Reviews of Modern Physics* 29.1 (1957). Sec. 6, p. 74.
- [2] D. T. Smithey et al. “Measurement of the Wigner distribution and the density matrix of a light mode using optical homodyne tomography: Application to squeezed states and the vacuum”. In: *Phys. Rev. A* 70 (1993), p. 1244.
- [3] K. Vogel and H. Risken. “Determination of quasiprobability distributions in terms of probability distributions for the rotated quadrature phase”. In: *Phys. Rev. A* 40 (1989), p. 2847.
- [4] T. J. Dunn, I. A. Walmsley, and S. Mukamel. “Experimental Determination of the Quantum-Mechanical State of a Molecular Vibrational Mode Using Fluorescence Tomography”. In: *Phys. Rev. Lett.* 74 (6 1995), pp. 884–887. DOI: 10.1103/PhysRevLett.74.884. URL: <http://link.aps.org/doi/10.1103/PhysRevLett.74.884>.
- [5] D. Leibfried et al. “Experimental Determination of the Motional Quantum State of a Trapped Atom”. In: *Phys. Rev. Lett.* 77 (21 1996), pp. 4281–4285. DOI: 10.1103/PhysRevLett.77.4281. URL: <http://link.aps.org/doi/10.1103/PhysRevLett.77.4281>.
- [6] D’Ariano, Paris, and Sacchi. “Quantum tomography”. In: *Advances in Imaging and Electron Physics* 128 (2003), pp. 205–308.
- [7] M. Paris and J. Řeháček. *Quantum States Estimation*. Lecture notes in Physics vol 649 Springer, Berlin, 2004.

BIBLIOGRAPHY

- [8] Welsch, Vogel, and Opatrny. “Homodyne Detection and Quantum State Reconstruction”. In: *Progress in Optics* 39 (1999), pp. 63–211.
- [9] A. Ferraro, S. Olivares, and M. G. A. Paris. *Gaussian states in quantum information*. Bibliopolis, Napoli, 2005.
- [10] Scully and Zubairy. *Quantum Optics*. Cambridge University Press, 1997.
- [11] Ulf Leonhardt. *Measuring the Quantum State of Light*. CAMBRIDGE STUDIES IN MODERN OPTICS, 1997.
- [12] Mark Fox. *Quantum Optics an introduction*. Oxford Master Series in Physics, 2006.
- [13] Ulf Leonhardt. *Quantum Optics*. CAMBRIDGE UNIVERSITY PRESS, 2010.
- [14] G. M. D’Ariano, C. Macchiavello, and M. G. A. Paris. “Detection of the density matrix through optical homodyne tomography without filtered back projection”. In: *Phys. Rev. A* 50 (5 1994), pp. 4298–4302. DOI: 10.1103/PhysRevA.50.4298. URL: <http://link.aps.org/doi/10.1103/PhysRevA.50.4298>.
- [15] G. M. D’Ariano, U. Leonhardt, and H. Paul. “Homodyne detection of the density matrix of the radiation field”. In: *Phys. Rev. A* 52 (3 1995), R1801–R1804. DOI: 10.1103/PhysRevA.52.R1801. URL: <http://link.aps.org/doi/10.1103/PhysRevA.52.R1801>.
- [16] Daniel F. V. James et al. “Measurement of qubits”. In: *Phys. Rev. A* 64 (5 2001), p. 052312. DOI: 10.1103/PhysRevA.64.052312. URL: <http://link.aps.org/doi/10.1103/PhysRevA.64.052312>.
- [17] Michael M. Wolf, Geza Giedke, and J. Ignacio Cirac. “Extremality of Gaussian Quantum States”. In: *Phys. Rev. Lett.* 96 (8 2006), p. 080502. DOI: 10.1103/PhysRevLett.96.080502. URL: <http://link.aps.org/doi/10.1103/PhysRevLett.96.080502>.
- [18] R. E. Slusher et al. “Observation of Squeezed States Generated by Four-Wave Mixing in an Optical Cavity”. In: *Phys. Rev. Lett.* 55 (22 1985), pp. 2409–2412. DOI: 10.1103/PhysRevLett.55.2409. URL: <http://link.aps.org/doi/10.1103/PhysRevLett.55.2409>.

-
- [19] Lvovsky and Raymer. “Continuous-variable optical quantum-state tomography”. In: *REVIEWS OF MODERN PHYSICS* 81.1 (2009), p. 299.
- [20] Hans A. Bachor and Timothy C. Ralph. *A Guide to experiments in Quantum Optics*. WILEY-VCH, 2004.
- [21] Hansen et al. “An ultra-sensitive pulsed balanced homodyne detector: Application to time-domain quantum measurements”. In: *OPTICS LETTERS* 26.21 (2001), p. 1714.
- [22] Haderka et al. “Fast time-domain balanced homodyne detection of light”. In: *Applied Optics* 48.15 (2009), pp. 2884–2889.
- [23] Cooper, Soller, and Smith. “High-stability time-domain balanced homodyne detector for ultrafast optical pulse applications”. 2011. URL: <http://arxiv.org/abs/1112.0875v1>.
- [24] Kumar et al. “Versatile Wideband Balanced Detector for Quantum Optical Homodyne Tomography”. 2011. URL: <http://arxiv.org/abs/1111.4012>.
- [25] Zavatta et al. “Time-domain analysis of quantum states of light: noise characterization and homodyne tomography”. In: *J. Opt. Soc. Am. B* 19.5 (2002), p. 1189.
- [26] Chi et al. “A balanced homodyne detector for high-rate Gaussian-modulated coherent-state quantum key distribution”. In: *New Journal of Physics* 13 (2011). Section 4.5, p. 013003.
- [27] Diels and Rudolph. *Ultrashort laser pulse phenomena*. (Section 8.2). ACCADEMIC PRESS, 1996.
- [28] Daniele Fausti. “Dinamiche elettroniche di superficie”. Università Cattolica Brescia, 2003.
- [29] URL: http://en.wikipedia.org/wiki/Kerr-lens_modelocking.
- [30] Yuemeng Chi. “High speed homodyne detector for gaussian-modulated coherent state quantum key distribution”. University of Toronto, 2009.
- [31] Appel et al. “Electronic noise in optical homodyne tomography”. In: *Physical Review A* 75.3 (2007), p. 035802.

BIBLIOGRAPHY

- [32] Okubo et al. “Pulse-resolved measurement of quadrature phase amplitudes of squeezed pulse trains at a repetition rate of 76 MHz”. In: *Opt. Lett.* 33 (2008), pp. 1458–1460.
- [33] Zavatta, Viciani, and Bellini. “Non-classical field characterization by high-frequency, time-domain quantum homodyne tomography”. In: *Laser Phys. Lett.* 3.1 (2006), pp. 3–16.
- [34] Wu Jinwei. “Applications of Optical Homodyne Tomography”. University of Science and Technology of China, 2000.
- [35] D. L. Andrews. “Representation of the pulsed output from a mode-locked laser using quantum field theory and an application in multiphoton ionisation”. In: *J. Phys. B* 11 (1978), p. 2665.
- [36] Wolfgang P. Schleich. *Quantum Optics in Phase Space*. Wiley-VCH, 2001.
- [37] Leonhardt and Paul. “MEASURING THE QUANTUM STATE OF LIGHT”. In: *Prog. Quant. Electr.* 19 (1995), pp. 84–130.
- [38] Chi et al. “A balanced homodyne detector for high-rate Gaussian-modulated coherent-state quantum key distribution”. In: *New Journal of Physics* 13 (2011).
- [39] Stefano Olivares. “Quantum optics in the phase space - A tutorial on Gaussian states”. In: *Eur. Phys. J. Special Topics* 203 (2012), pp. 3–24.
- [40] Braustein. “Homodyne statistics”. In: *Phys. Rev. A* 42 (1990), p. 474.
- [41] Breitenbach, Schiller, and Mlynek. “Measurement of the quantum states of squeezed light”. In: *Nature* 387 (1997), pp. 471–475.
- [42] D’auria, Chiummo, and Lurentis. In: *Opt Express* 13 (2005), p. 948.
- [43] Di Noia Maurizio. “Entanglement concentration and distillation in continuous variable systems”. Università degli Studi di Milano, Facoltà di Scienze Matematiche, Fisiche e Naturali, 2005-2006.

Ringraziamenti

I primi ringraziamenti vanno alle persone che mi hanno seguita nel corso di questa tesi. Il mio relatore, Daniele Fausti, per l'attenzione con cui mi ha guidata nel corso dell'attività di laboratorio, dandomi la possibilità di comprendere e gestire le diverse problematiche sperimentali e le possibili soluzioni, senza fornirmi "ricette pronte" ma permettendomi di acquisire con i miei tempi le competenze sperimentali necessarie; lo ringrazio in particolare per avermi trasmesso la sua genuina passione per la scienza, che ha reso sempre interessante e costruttivo il lavoro insieme. Stefano Olivares, Fabio Benatti e Roberto Floreanini, che hanno coordinato la parte teorica della tesi e l'analisi dati; grazie al loro supporto scientifico è stato possibile formulare una trattazione matematica che permette di descrivere lo stato quantistico della luce emessa da un laser impulsato, su cui pochissimo è pubblicato in letteratura; li ringrazio in particolare per la pazienza e la disponibilità con cui mi hanno guidata e per i preziosi consigli nel corso della stesura dell'elaborato. Fulvio Parmigiani, per i confronti sempre costruttivi, e tutti i componenti del gruppo di ricerca *T-Rex* da lui coordinato; in particolare Fabio Novelli e Federico Cilento per il grande aiuto in laboratorio e nella scrittura del software di gestione dell'apparato sperimentale.

Mi ritengo molto fortunata per aver contribuito nel mio piccolo, con questa tesi, al progetto di ricerca teorico-sperimentale che vede coinvolte le persone appena citate. Poter partecipare, con loro, ad incontri, seminari e dibattiti nel corso di questi mesi è stato per me estremamente formativo; le tante cose imparate costituiranno un importante bagaglio scientifico, qualsiasi sarà il mio futuro professionale.

Ringrazio il collegio universitario *L. Fonda* ed *Elettra* s.p.a., che hanno finanziato la mia borsa di studio. Mi auguro che tale iniziativa prosegua nei prossimi anni, per permettere a studenti meritevoli di studiare in un ambiente stimolante per la Fisica quale è Trieste senza troppo gravare economicamente sulle proprie famiglie.

Ringrazio la mia di famiglia, i miei genitori che mi hanno sempre sostenuta e mio fratello, per sopportarmi, per venirmi a prendere ogni volta alla stazione e per un sacco di altre cose... :) ...tra cui l'aiuto con la presentazione. Gli amici di sempre, quelli con cui, quando torno a casa, non vedo l'ora di andare a bere una birra e chiacchierare; gli amici conosciuti in questa esperienza a Trieste, la loro compagnia ha arricchito questi due anni di sorrisi, risate, canzoni, mangiate ed avventure, grazie a loro posso dire non solo di aver studiato a Trieste, ma di averci vissuto. Infine, ringrazio infatti questa città, luogo dell'anima, dove ho incontrato il mio compagno, mia terra e mia pace.